



Effects of South-to-North Water Diversion Project on groundwater and land subsidence in Beijing, China

Kunchao Lei^{1,2} · Fengshan Ma¹ · Beibei Chen³ · Yong Luo² · Wenjun Cui² · Long Zhao² · Xinhui Wang² · Aihua Sun²

Received: 25 April 2022 / Accepted: 17 November 2022 / Published online: 19 December 2022
© Springer-Verlag GmbH Germany, part of Springer Nature 2022

Abstract

The South-to-North Water Diversion Project Central Route (SNWDP-CR) is the largest water control project which has ever been built, and the aim of which is to optimize the reallocation of water resources from South China to North China. Since it was put into operation in December 2014, it has delivered more than 6×10^9 m³ of water to Beijing, which has changed the water supply pattern in Beijing and provided conditions for reducing groundwater extraction and controlling land subsidence. In this study, a variety of monitoring data are used to analyze the changes of the groundwater flow field, groundwater level, land subsidence, soil deformation, and hydrogeology parameters before and after the SNWDP-CR. The study showed that the groundwater level of the first to fourth aquifer groups rose on average by 2.72 m, 3.68 m, 3.31 m, and 1.91 m from 2015 to 2020. The average subsidence rate decreased from 18.8 mm/year in 2015 to 10.85 mm/year in 2020. The deformation characteristics of different lithological soil layers under different water level change modes can be summarized into 4 categories. The sand layer is mainly characteristic of elastic deformation. The cohesive soil layers of different depths have elastic, plastic, and creep deformation, and the viscoelastic-plastic characteristics are obvious. For different stages of soil deformation, the changes of elastic and inelastic skeletal specific storage rates are not constant. As the groundwater level decreases, the soil skeletal specific storage rate shows a decreasing trend.

Keywords Water Diversion Project · Groundwater level · Land subsidence · Deformation characteristic · Skeletal specific storage rate

Introduction

Land subsidence is an environmental geological phenomenon caused by the overexploiting underground resources such as groundwater, which can bring about disasters in severe cases (Hu et al. 2004; Motagh et al. 2008; Galloway and Burbey 2011; Gambolati and Teatini 2015; Guzy and Malinowska 2020). There are 34 countries and about 200 cities around the world which have experienced land subsidence (Herrera-García et al. 2021). For example, the San Joaquin

and Santa Clara basins in the USA (Galloway et al. 1998; Pavelko et al. 2006; Jeanne et al. 2019); Tokyo and Osaka in Japan (Cao et al. 2020); Mexico City in Mexico (Strozzi and Wegmuller 1999; Chaussard et al. 2014b); Venice in Italy (Tosi et al. 2007; Teatini et al. 2010); Bangkok in Thailand (Phien Wej et al. 2006); Jakarta in Indonesia (Abidin et al. 2008, 2011); and Shanghai, Tianjin, and Beijing in China (Hu et al. 2009; Xu et al. 2012; Gong et al. 2018).

In China, more than 22 provinces (cities) suffer from land subsidence (Xue et al. 2005). The area with cumulative land subsidence greater than 200 mm added up to 90,000 km² in 2012 (Ye et al. 2016b). Land subsidence permanently reduces aquifer-system storage capacity, causes earth fissures, damages buildings and civil infrastructure, and increases the susceptibility and risk of flood (Tomas et al. 2011; Pacheco-Martinez et al. 2013; Miller and Shirzaei 2015; Zhu et al. 2015; Zhang et al. 2016; Chen et al. 2020). Land subsidence, which is characteristic of long formation time, wide range of influence, as well as difficulty in prevention and recovery, etc., has become a global and comprehensive environmental geological problem that has a

✉ Fengshan Ma
fsma@mail.iggcas.ac.cn

¹ Key Laboratory of Shale Gas and Geoengineering, Institute of Geology and Geophysics, Chinese Academy of Sciences, Beijing 100029, China

² Beijing Institute of Geo-Environment Monitoring, Beijing 100195, China

³ College of Resource Environment and Tourism, Capital Normal University, Beijing 100048, China

serious impact on the human living environment (Guzy and Malinowska 2020; Herrera-García et al. 2021).

Beijing, capital of China which has a serious shortage of water, is located in North China and has a population of more than 21 million. According to public surveys from the Beijing Water Authority of China, the average available water resource per person is less than 300 cubic meters per year, which is only 1/8 of that of the nation (Shao 2007). There is about 50% to 70% of the water supply comes from groundwater in Beijing (Chen et al. 2020; Lei et al. 2022). Long-term overexploitation of groundwater resources has brought about serious problems of land subsidence in Beijing (Lei et al. 2016; Chen et al. 2019; Zhu et al. 2020). The annual subsidence rate peaked at about 156 mm/year in the eastern part of Beijing Plain from 2010 to 2015 (Zhang et al. 2016). The area affected by a cumulative subsidence larger than 100 cm was more than 300 km² between 1955 and 2015, which seriously affected the safety of the infrastructure operation (Lei et al. 2016).

The South-to-North Water Diversion Project (SNWDP) is the largest water control project which has ever been built, and the aim of which is to optimize the reallocation of water resources from South China to North China (Bai and Liu 2018). The South-to-North Water Diversion Project Central Route (SNWDP-CR) diverts water from the Danjiangkou reservoir (32° 43' North, 111° 34' East) on the Han River via artificial canals that cross Henan and Hebei Provinces to the Tuancheng Lake of Beijing (39° 55' North, 116° 24' East). The SNWDP-CR, the total length of which is about 1300 km, spans the four provinces or cities including Henan, Hebei, Beijing, and Tianjin. The SNWDP-CR, which began to be constructed in 2003, and was put into operation in December 2014, is supposed to relieve, to some degree, the partial pressure of water demand in Beijing Plain. The cumulative water volume released to Beijing amounted to 6.0 × 10⁹ m³ by December 2020. From 2014 to 2020, the average of groundwater level rose by 2.9 m in Beijing Plain (Lei et al. 2020).

At present, some scholars have carried out abundant research on the impact of water transfer projects, groundwater exploitation management and artificial recharge on groundwater environment and ecological changes (Yang et al. 2012; Zhao et al. 2017), groundwater level changes (Zhang et al. 2014, 2018; Ye et al. 2014; Li et al. 2017; Chen et al. 2020), and control of land subsidence (Zhang et al. 2015; Wei et al. 2022). Several years after the SNWDP-CR operation, the groundwater level has altered from continuous decline to gradual rise in many areas of the Beijing plain (Zhang et al. 2018; Lei et al. 2020; Du et al. 2021). However, there are few comprehensive analyses on the groundwater flow field and land subsidence during the process of the groundwater level in the Beijing Plain changing from decline to rise before and after the operation

of SNWDP-CR. Therefore, a variety of monitoring data, in this study, are used to analyze the groundwater flow field and land subsidence changes in the Beijing Plain before and after the SNWDP-CR operation and to study the stress–strain characteristics and the changes of hydrogeological parameters of soil layers at different depths under different water level change modes. This is of great significance for the further investigation of the mechanism of land subsidence, the determination of the constitutive relationship of soil layer deformation, and realization of the accurate simulation of land subsidence and the scientific regulation of groundwater.

The objectives of this study are as follows: firstly, to compare the evolution of the groundwater flow field and the change of groundwater level by using the regional groundwater level observation data; secondly, to obtain the evolution characteristics of the land subsidence before and after the SNWDP-CR operation by using Persistent Scatterer Interferometry (PSI) technique; and thirdly, to study the deformation characteristics of water bearing sand layers and different compression layer groups under different water level change modes by using long-time series extensometer and groundwater level data. The soil mechanics test is used to simulate and verify the deformation of the soil layer and, fourthly, to analyze the changes of hydrogeological parameters at different stages of soil deformation by calculating the elastic and inelastic skeletal specific storage rate of the sand layer and compressed layer group before and after the SNWDP-CR operation.

Description of the study area

Geology and hydrogeology

Beijing is located on the northwestern edge of the North China Plain. The terrain is generally higher in its northwest part and lower in its southeastern part. It is surrounded by the Taihang Mountains in the west, the Yanshan Mountains in the north, and the inclined plain in the southeast. The geographical coordinates of Beijing are E115.7°–117.4° and N39.4°–41.6°. The total area of Beijing is 16,410 km², and the plain area is 6400 km². The plain area accounts for about 39% of the total area of the city (Wei et al. 2008). It is characterized by a continental monsoon climate, with an average annual precipitation of 570 mm/year (1961–2020). Eighty percent of the precipitation is concentrated in the period mid-June to September. The average annual temperature is around 11.7 °C, and the maximum value may reach up to 42.6 °C in summer.

The Quaternary stratum of Beijing Plain is mainly formed by the alluvial-diluvial effect of five rivers, which are Yongding, Chaobai, Beiyun, Daqing, and Jiyun rivers. On the top of the alluvial region, the thickness of the Quaternary

is about 20–40 m. The lithology is a single layer of sand, gravel, or a thin layer of cohesive soil on the top of sand and gravel in some areas (Cai et al. 2009). In the middle and lower parts of alluvial regions and alluvial plain, the thickness of the sediment increases, the layers increase, and the soil particles gradually change from coarse to fine. The lithology is that sand, gravel, and cohesive soil layers appear alternately, and the cohesive soil is dominant. In the center of the Quaternary sedimentary depression, the thickness of the Quaternary reaches more than 1000 m (Lei et al. 2016, 2022) (Fig. 1).

The aquifer system in the Beijing Plain can be divided in the vertical direction into three main aquifer groups. The first aquifer group (unconfined aquifer and shallow confined aquifer) are the Quaternary Holocene (Q4) and Upper Pleistocene (Q3) alluvial deposits, the bottom depths of which are about 25 m and 80–120 m respectively. The second aquifer group (medium-deep confined aquifers) is a multi-layered structure of the Quaternary Middle Pleistocene (Q2) strata,

the lithology of which is mainly medium-coarse sand, partly with gravel, and the bottom depth of which is about 180 m. The third aquifer group (deep confined aquifers) is the Lower Pleistocene (Q1) stratum of the Quaternary System with a multi-layer structure, which is dominated by medium-coarse sand and gravel, and the bottom boundary of which is the Quaternary basement or about 260–300 m (Jia et al. 2007). At the same time, the division of compression layer group and the division of aquifer group have an obvious corresponding relationship in Beijing Plain (Figs. 2 and 3).

The history of groundwater exploitation and land subsidence development

The occurrence and development of land subsidence have an obvious corresponding relationship with the history of groundwater exploitation (Fig. 4). The period from 1955 to 1973 was the initial exploitation of groundwater and the formation stage of land subsidence. During this period, the

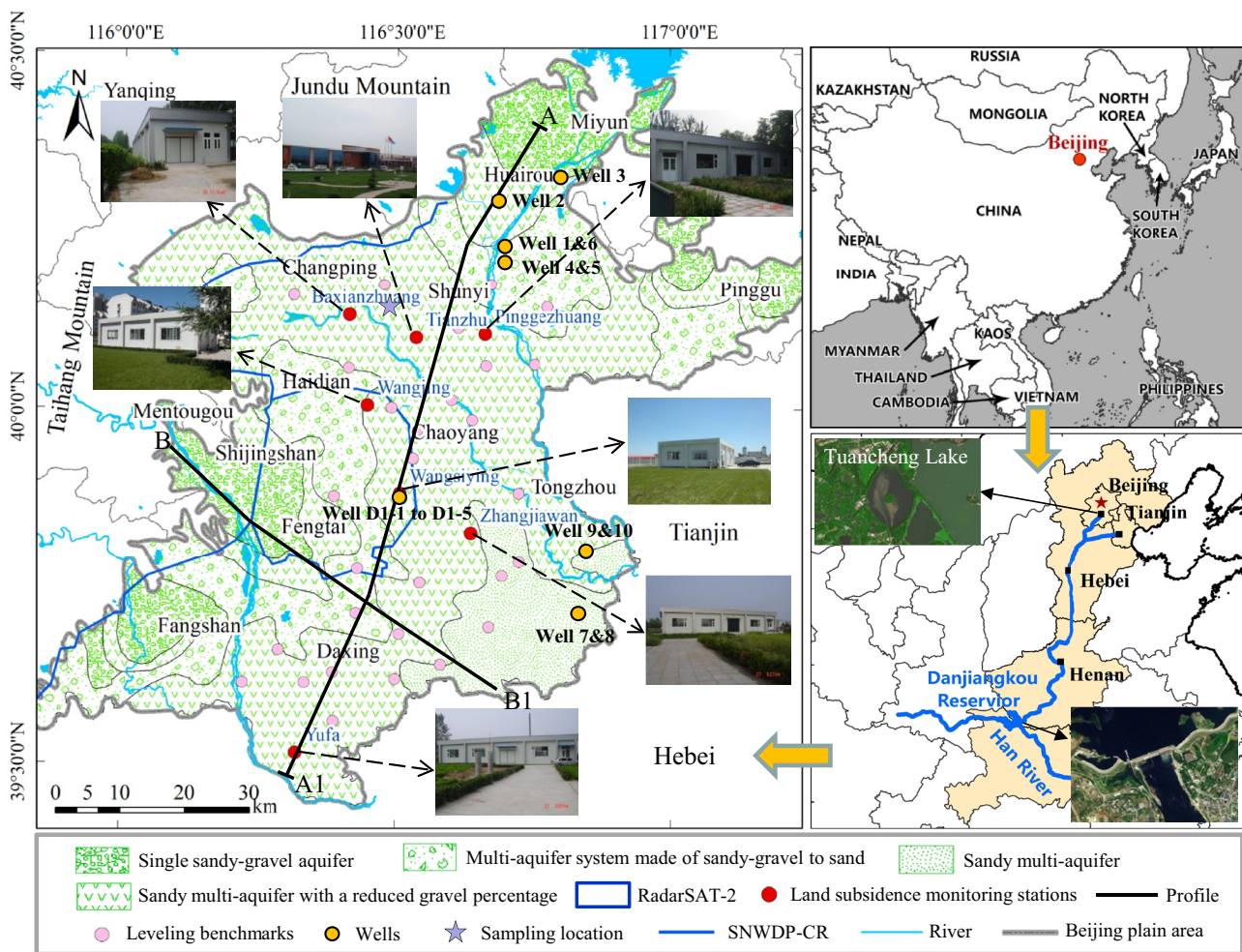
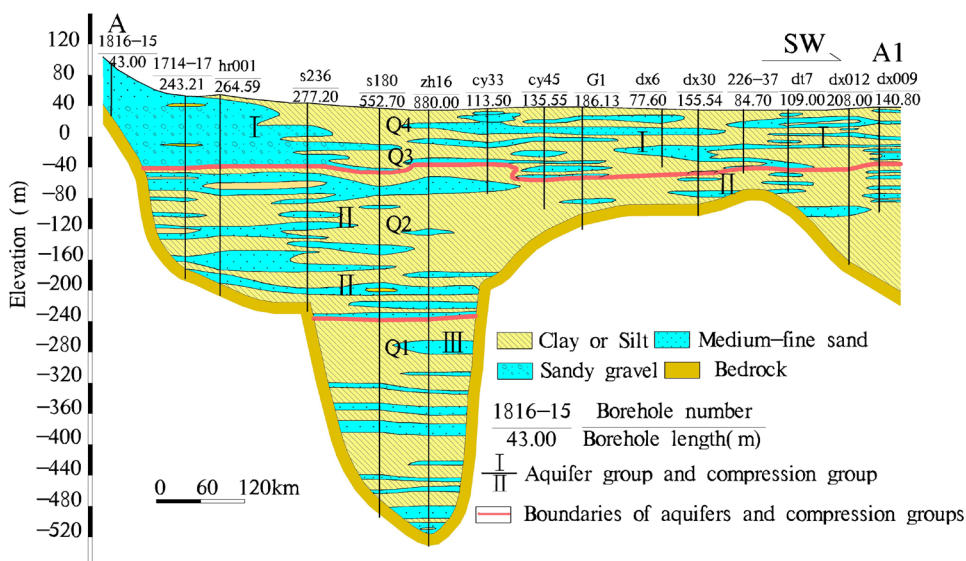


Fig. 1 The location of study area and the lithology zone of aquifer. The position of levelling benchmarks, extensometer stations, and groundwater monitoring wells are provided. The SNWDP-CR route is marked with a blue color in the bottom right panel

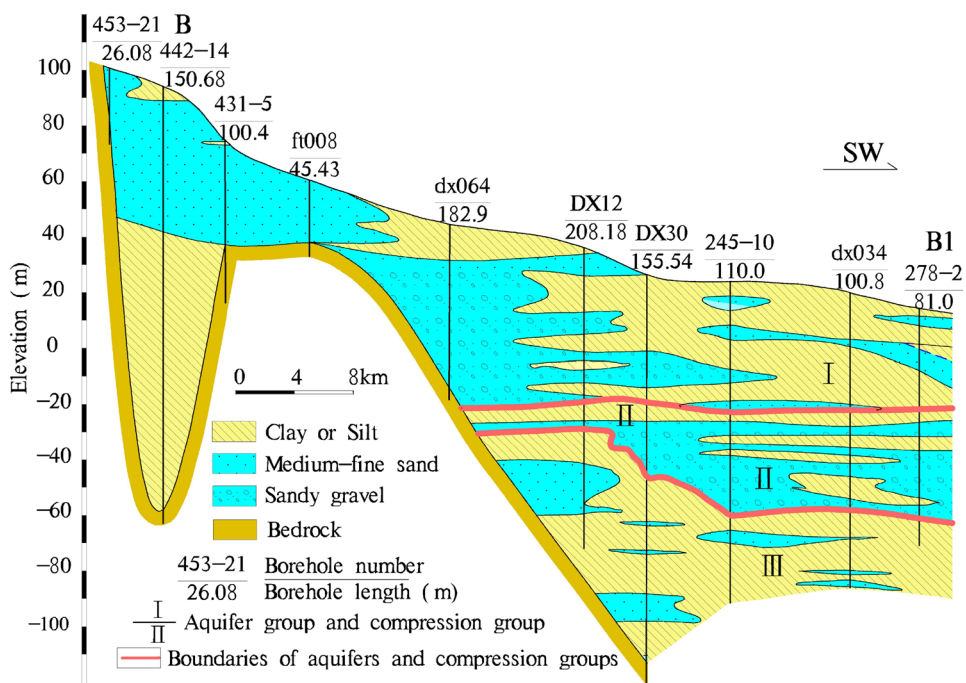
Fig. 2 Hydrogeological cross-section A–A1 (the location is indicated in Fig. 1)



amount of groundwater extraction in Beijing was small. The land subsidence only occurred in the groundwater over-exploitation area, with the land subsidence rate being a few millimeters per year. The period from 1973 to 1983 was the stage of increase of groundwater exploitation and development of land subsidence. During this period, the amount of groundwater exploitation in Beijing remained at 2.5–2.8 billion m³ per year, and the annual average land subsidence rate being 18–30 mm/year. The period from 1983 to 1999 was the stage of stability of groundwater exploitation and expansion of land subsidence. During this period, the amount of

groundwater extraction was relatively stable, with an average annual extraction volume of about 2.6 billion m³. The over-extraction area accounted for more than 70% of the plain. The area of land subsidence expanded significantly, with an average annual subsidence rate of 19–24 mm/year. The period from 1999 to 2015 was the rapid development stage of land subsidence. During this period, Beijing experienced the longest dry year in history. The amount of groundwater exploitation declined slightly, but the exploitation horizon gradually extended to deeper layers. During this period, the groundwater in Beijing was severely depleted, and the land

Fig. 3 Hydrogeological cross-section B–B1 (the location is indicated in Fig. 1)



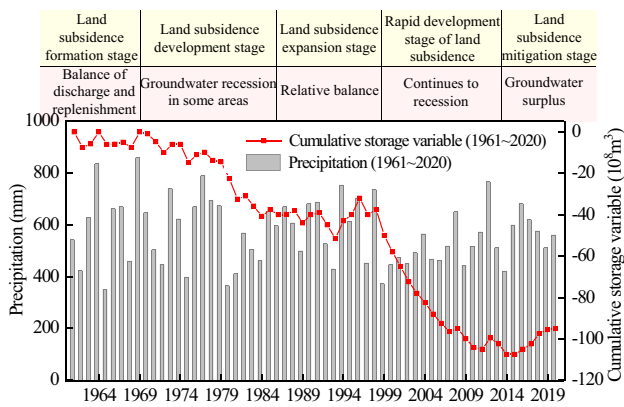


Fig. 4 The relationship between the accumulated storage variables of groundwater and the precipitation and the division of land subsidence in Beijing

subsidence developed rapidly, with a maximum subsidence rate of 156 mm/year (Jia et al. 2018). Since 2015, with the South-to-North Water Diversion Project Central Route was officially operated, the amount of groundwater exploitation in Beijing has decreased, from 2.0 billion m³ in 2014 to 1.35 billion m³ in 2020. At this stage, the land subsidence has been gradually slowing down, with an average annual subsidence rate of 11–19 mm/year (Fig. 5).

Dataset and methodology

Dataset

To quantify the impact of the water resource supplied by SNWDP-CR on the Beijing groundwater flow field, groundwater level, land subsidence, soil deformation, and hydrogeological parameters, the remotely sensed

Table 1 Acquisition parameters of Radarsat-2 datasets

SAR sensor	Radarsat-2
Orbit direction	Descending
Orbit altitude	798 km
Band (wavelength)	C-band (5.6 cm)
Revisit cycle	24 days
Spatial resolution	30 m
Incidence angle (°)	27.8
Polarization	VV
Centre Location	40.20 116.40
Number of images	72
Temporal coverage	2013/01/16–2020/12/22

measurements, levelling and extensometer data, groundwater level data, geotechnical test, and aquifer recharge management data have been gathered, and the dataset has been revised in the following paragraphs Table 1.

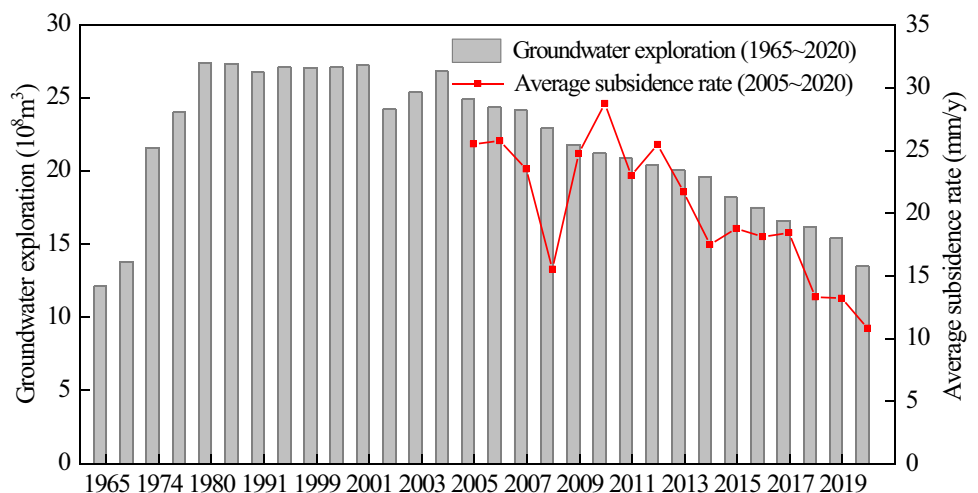
Remotely sensed data

PSI technique outcomes were obtained by processing Radarsat-2 acquisitions. A total of 72 Radarsat-2 images with 30-m resolution and 24-day revisit time acquired in Stripmap mode from January 2013 to December 2020 were processed. These stacks of Synthetic Aperture Radar (SAR) images were used to map land subsidence over the period from 2013 to 2020, respectively. The acquisition parameters of SAR images are presented in Table 2.

In situ deformation data

The different-depth extensometers in the seven land subsidence monitoring stations and thirty levelling benchmarks

Fig. 5 Curve of relationship between groundwater extraction volume and average subsidence rate in Beijing



were used in the study area (Fig. 1). The levelling results were used to calibrate and validate the land movements derived from PSI. The extensometer data recorded from 2006 to 2020 or from 2009 to 2020 were selected to analyze the main subsidence contribution layer and the relationship between layered soil deformation and groundwater level.

Groundwater level data

The comparative maps of the groundwater level of different aquifer groups in the Beijing Plain from 2015 to 2020 are drawn by virtue of the contour data of groundwater level in 2015 and 2020. A long-term series of groundwater level change curves are drawn by means of the monitoring data from 15 groundwater wells in the northern, eastern, and southeastern plains. The change trend of groundwater flow field and groundwater level in different aquifer groups before and after the SNWDP-CR operation has been analyzed. The location of the well is shown in Fig. 1. Well-1, Well-2, and Well-3 are located in a single aquifer group in the northern part of the plain. The lithology is mainly sand and gravel, and the depths of the wells are 45 m, 60 m and 89 m, respectively. Well-4, Well-5, and Well-6 are located near the channel of the Chaobai River in the northern part of the plain. The aquifer group is a single-structure sandy gravel layer, and the depths of the wells are 50 m, 100 m, and 60 m, respectively. D1-1, D1-2, D-3, D-4, and D1-5 wells are located in the Wangsiying land subsidence monitoring station in the eastern part of the plain. The aquifer group is a multi-layer structure composed of sand and cohesive soil, and the depths of the wells are 185 m, 155 m, 102 m, 54 m, and 19 m, respectively. Well-7, Well-8, Well-9, and Well-10 are located in the southeastern part of the plain. The aquifer group is a multi-layer structure composed of sand and cohesive soil, and the depths of the wells are 182 m, 300 m, 166 m, and 300 m, respectively. At the same time, the groundwater level data of seven land subsidence monitoring stations, recorded from 2006 to 2020 or from 2009 to 2020, are selected to analyze the relationship with the extensometer data.

Managed aquifer recharge

The dataset related to the managed aquifer recharge position, duration, and volume of water supplied by the SNWDP-CR were collected from 2015 to 2020. The data were used to analyze the measured changes of the groundwater level. A typical area where the water supplied by the SNWDP-CR was used to recharge the aquifer in the northern plain. The location is shown in Fig. 6. The remote sensing image data in Fig. 6 are downloaded in Google Earth.

Undisturbed soil sample test data

A borehole with a depth of 100 m was constructed in the northern part of the plain, and it was numbered ZK01. Undisturbed soil samples were collected in the borehole for geotechnical tests. The numbers of the tested soil sample were Nos. 4, 6, 7, 9, 13, 16, and 21, respectively. Basic physical property tests and standard consolidation tests were carried out for each soil sample. In addition, loading tests of step by step were carried out in No. 7 and No. 9 soil samples, unloading tests of step by step were carried in No. 4 and No. 13 soil samples, and repeated loading and unloading tests in No. 6, No. 16, and No. 21 soil samples. The depth of soil sample collection and test items are shown in Table 2.

Methodologies

By combining PSI, GIS spatial analysis, stress–strain analysis, mathematical statistics, and geotechnical test methods, this paper studies the changes of groundwater flow field, groundwater level, land subsidence, soil deformation characteristics, and hydrogeological parameters before and after the SNWDP-CR operation. Firstly, the regional groundwater level contour data are utilized to draw the comparative map of the groundwater level of different aquifer groups in the Beijing Plain from 2015 to 2020. By combining the data of multiple groundwater wells, the changes in the groundwater flow field and groundwater level before and after the SNWDP-CR operation are analyzed by means of GIS and mathematical



Fig. 6 The water supplied by the SNWDP-CR was used to recharge the aquifer in the Huai and Chaobai River channels in the northern part of the plain. **a** The remote sensing image of the rubber dam and river channel before the aquifer recharge in April 2020. **b** The remote sensing image of the rubber dam and river channel after the aquifer recharge in August 2020. **c** Rubber dam in Niulanshan. **d** Recharge the aquifer by using the Chaobai River channel

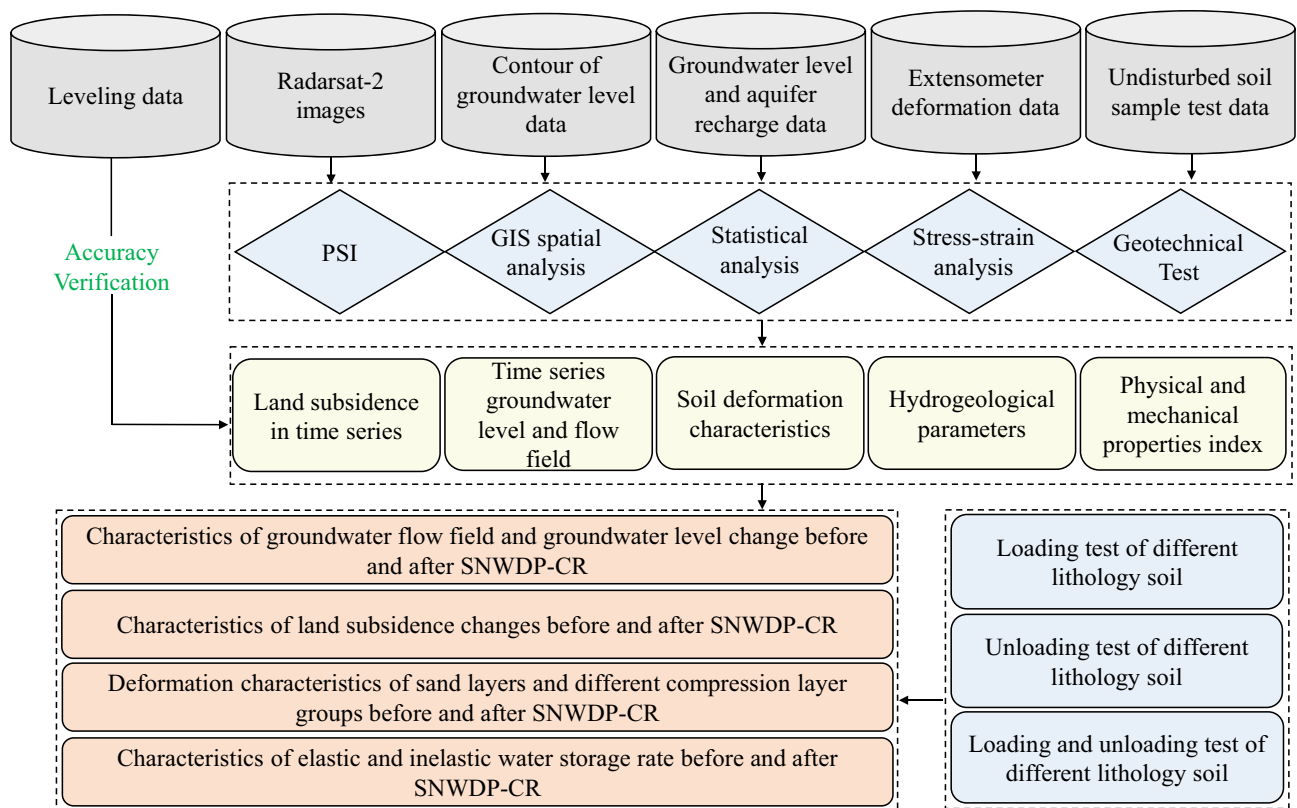


Fig. 7 The flowchart of methodologies

statistics methods. Secondly, Radarsat-2 images, by means of PSI technique, are processed to obtain the long-term sequence of land subsidence distribution characteristics in the Beijing Plain. The relationship between the changes of groundwater level and land subsidence before and after the SNWDP-CR operation is analyzed. Thirdly, by using the extensometer and groundwater level data in the land subsidence monitoring station, the stress–strain analysis method is used to study the deformation characteristics of the sand layer and different compression layer groups under the different groundwater level change mode before and after the SNWDP-CR operation. Verification of soil layer deformation are carried out by using geotechnical

tests. Fourthly, the elastic and inelastic skeletal specific storage rate of the sand layer and different compression layer groups are calculated before and after the SNWDP-CR operation. Besides, the changes of related hydrogeological parameters in different stages of soil deformation are analyzed. The overall technical framework is shown in Fig. 7.

PSI technique

The basic idea of PSI is to select those pixels as the research object that maintain high coherence in the long-term sequence of SAR images, and the long-term sequence

Table 2 The depth and test items of the soil samples

Number	Sampling depth (m)	Lithology	Test items
4	22.0–22.2	clay	Basic physical property test, standard consolidation test, unloading test
6	36.0–36.2	clay	Basic physical property test, standard consolidation test, loading and unloading test
7	43.0–43.2	clay	Basic physical property test, standard consolidation test, loading test
9	51.0–51.2	silt	Basic physical property test, standard consolidation test, loading test
13	56.6–56.8	silt	Basic physical property test, standard consolidation test, unloading test
16	66.5–66.7	silty clay	Basic physical property test, standard consolidation test, loading and unloading test
21	73.0–73.2	silt	Basic physical property test, standard consolidation test, loading and unloading test

stability of them enables the accurate phase information to be obtained. By separating the phase of each coherent target point, including the elevation, the orbit, and the phase change of the atmosphere, the surface deformation can be obtained. This method can effectively overcome the influence of space and time decorrelation and atmospheric delay of DInSAR and improve the monitoring accuracy of surface deformation, which can reach the millimeter level. PSI technique was first developed by Ferretti (Ferretti and Prati 2000; Ferretti et al. 2001), and since then it has largely been used to measure movements of Earth surface (Galloway et al. 1998; Hoffmann et al. 2001, 2003; Ng et al. 2012; Gong et al. 2018; Malinowska et al. 2019; Strozzi et al. 2020; Chen et al. 2020). The main steps of the PSI processing chain are as follows: selection of a master image from the available series of SAR scenes, construction of a series of interferograms, selection of permanent scatterers (PS) of the radar signal according to amplitude dispersion index and coherence thresholds, and phase unwrapping. The differential interferometric phase Φ_{PS} of each PS in the interferogram can be expressed as the accumulation of five components (Hooper et al. 2004):

$$\Phi_{PS} = \Phi_{def} + \Phi_{top} + \Phi_{atm} + \Phi_{orb} + \Phi_n \quad (1)$$

In the formula, Φ_{def} is the deformation phase along the line of sight, Φ_{top} the topographic phase, Φ_{atm} the phase component due to atmospheric delay, Φ_{orb} the orbital error phase, and Φ_n the phase noise. The deformation phase Φ_{def} of PS can be separated from the other components. An external DEM with resolution of 30 m is used to remove Φ_{top} from the interferometric phase. The phases due to atmosphere delay and noise are removed through filtering processes (Teatini et al. 2007). In this paper, GAMMA software is used to process 72-scene Radarsat-2 images for time-series differential interference processing and PS point extraction. Interferometric image pairs with a baseline distance of more than 300 m are eliminated, and 30 m resolution SRTM data are used as the reference DEM. After removing the terrain phase, geocoding and transforming the line of sight (LOS) to the vertical projection, the vertical deformation rate of the ground surface in the Beijing Plain area from 2013 to 2020 is obtained. The projection formula of the line of sight (LOS) to the vertical projection is as follows:

$$V = \frac{V_{LOS}}{\cos\varphi} \quad (2)$$

where V and V_{LOS} represent the displacement rate along the vertical and LOS directions, respectively, and φ is the incidence angle of the InSAR.

The outcomes of the Radarsat-2 were calibrated by virtue of the thirty levelling benchmarks shown in Fig. 1 and the calibration was carried out by using the average annual

displacement rates over the period of investigation. Because of the lack of PS at the benchmarks, the average movement of the radar targets in a 100 m buffer zone around the levelling points was used as PSI value in the calibration procedure. The difference range of them is from 2 to 8 mm, with the mean square error being 5.16 mm (Table 3).

Estimation of water storage rate

The water storage rate refers to the amount of water stored or released from a unit volume of soil when the groundwater level rises or falls by one unit. Supposing that the amount of water stored or released by the soil layer is all converted into the volume change of the soil layer, and the soil layer only undergoes vertical displacement, the water storage rate reflects the vertical deformation of the soil layer per unit thickness when the water level changes by one unit and can be used to characterize the potential deformation of the soil layer. However, the concept of the water storage rate depicted above can only quantitatively describe the linear elastic deformation of the soil layer, but cannot describe the general residual deformation of the soil layer. Therefore, the concept of the water storage rate should be expanded and should be divided into the elastic skeletal specific storage rate and the inelastic skeletal specific storage rate (Helm 1975; Liu and Helm 2008a, b). When the effective stress of the aquifer is less than the preconsolidation pressure, the aquifer assumes the recoverable elastic deformation. By contrast, when the effective stress of the aquifer is greater than the preconsolidation pressure, the aquifer shows the irreversible inelastic deformation, that is, the plastic one. Now that the preconsolidation pressure is the largest effective stress in the history of the soil layer; it can correspond to the lowest water level of the aquifer and can be determined through the historical monitoring data. Therefore, if the groundwater level is lower than the water level corresponding to the preconsolidation pressure, the water storage rate is called inelastic skeletal specific storage rate; otherwise, it is called elastic skeletal specific storage rate. The formula can be expressed as follows:

$$S_{sk} = \begin{cases} S_{ske} = \frac{\Delta b}{b_0 \Delta h} (h \geq h_{min}) \\ S_{skv} = \frac{\Delta b}{b_0 \Delta h} (h < h_{min}) \end{cases} \quad (3)$$

In the formula, S_{ske} is the elastic skeletal specific storage rate (m⁻¹), S_{skv} is the inelastic skeletal specific storage rate (m⁻¹), Δb the amount of deformation (m), Δh the amount of water level change (m), b_0 the initial thickness of the soil layer (m), h the groundwater level (m), and h_{min} the lowest groundwater level in the previous period (m). Based on in situ data, Riley showed that aquifer system elastic and inelastic skeletal specific storage rate can be estimated from stress–strain diagrams (Riley 1969). The stress–strain

diagram method uses effective stress or water head as the ordinate axis and vertical strain or displacement as the abscissa axis to draw the relationship curve between the stress (water level) and strain (displacement). Then, according to the relationship curve, the elastic skeletal specific storage rate S_{ske} and the inelastic skeletal specific storage rate S_{skv} are successively calculated. The calculation method can refer to the following documents (Riley 1969; Helm 1975; Liu and Helm 2008a, b; Chaussard et al. 2014a; Motagh et al. 2017).

GIS spatial analysis and stress–strain analysis

The GIS spatial analysis method was used to compile the groundwater level comparison map of different aquifer groups in the Beijing Plain in 2015 and 2020. Combining the data of multiple groundwater wells, the characteristics of groundwater flow field and the changes of groundwater level before and after SNWDP-CR were analyzed. The stress–strain analysis method is used to study the deformation characteristics of the sand layer and different compression layer groups under the different groundwater level change mode before and after SNWDP-CR.

Geotechnical test

In order to further analyze and verify the deformation characteristics of different depths and different lithological soil layers in repeated rise and fall of the groundwater level, the loading, unloading, repeated loading, and unloading test methods are carried out to analyze different soil samples. The test is divided into three groups, and the loading, unloading, and repeated loading and unloading tests are carried out respectively. In each group of tests, clay and silt are used to make comparison, and silty clay is also selected to make comparison in repeated loading and unloading tests. With the load-deformation and deformation-time relationship curves drawn, the deformation characteristics and creep effects of different lithological soil layers under different loading and unloading modes are further analyzed.

No. 7 and No. 9 soil samples are subjected to loading test. The load is added from 25 to 1600 kPa, and the loading ratio is 1, i.e., 25 kPa, 50 kPa, 100 kPa, 200 kPa, 400 kPa, 800 kPa, and 1600 kPa.

No. 4 and No. 13 soil samples are subjected to unloading tests. Firstly, the first-level load imposed on the soil samples is added to 400 kPa and then unloaded to 50 kPa when the soil samples reach deformation stability, i.e., 400 kPa, 300 kPa, 200 kPa, 150 kPa, 100 kPa, and 50 kPa.

No. 6, No. 16, and No. 21 soil samples are subjected to loading and unloading tests. The first loading and unloading

cycle is as follows: 100 kPa, 200 kPa, 100 kPa, 200 kPa, and 100 kPa. The second loading and unloading cycle is as follows: 100 kPa, 400 kPa, 200 kPa, 400 kPa, and 200 kPa. The third loading and unloading cycle is as follows: 200 kPa, 800 kPa, 400 kPa, 800 kPa, and 400 kPa. The fourth loading and unloading cycle is as follows: 400 kPa, 1600 kPa, 800 kPa, 1600 kPa, and 800 kPa.

Results and discussion

Changes of groundwater flow field and groundwater level

The comparison of groundwater level of different aquifer groups in 2015 and 2020 are shown in Fig. 8. From 2015 to 2020, the groundwater level of different aquifer groups in most areas of the Beijing Plain rose significantly, such as the northern part of the plain area (Shunyi, Changping, and Pinggu District), the urban area, the eastern part of the plain (parts of Chaoyang), and the northern part of Daxing District. However, the groundwater level of different aquifer groups in the southeast of Tongzhou and the southern part of Daxing continued to decline (Fig. 8). The comparison of groundwater level changes in different aquifers in 2015 and 2020 is shown in Table 4.

The groundwater level change curves of 6 monitoring wells in the northern plain are showed in Fig. 9a, b. It can be seen from the figure that the groundwater level began to rise from 2015. By the end of 2020, the groundwater levels of 1, 2, and 3 wells had risen by 21.62 m, 21.72 m, and 17.24 m, respectively; the groundwater levels of 4, 5, and 6 wells by 2.11 m, 12.59 m, and 23.15 m, respectively. The groundwater level change curves in Wangsiying land subsidence monitoring station in the east of the plain are shown in Fig. 9c. Before 2017, the groundwater level of each aquifer group showed a continuous downward trend, with an average annual decline of 0.13–1.82 m. After 2017, the groundwater level of each aquifer group changed from decline to rise, with an average annual rise of 0.45–1.87 m. This is mainly because after the operation of SNWDP-CR, the reduction and conservation of groundwater were carried out in the emergency-type groundwater source fields of Miyun, Huairou, and Shunyi. The groundwater extraction in these areas decreased by two-thirds. At the same time, the SNWDP-CR supplies water to emergency water source fields through the Chaobai River. By the end of 2020, more than 5×10^8 m³ of groundwater has been recharged in this area. The groundwater level in the northern part of the plain has risen significantly. On the contrary, in parts of Tongzhou and Daxing which are sited in the southeast and south of the plain, the groundwater level was still declining. The groundwater

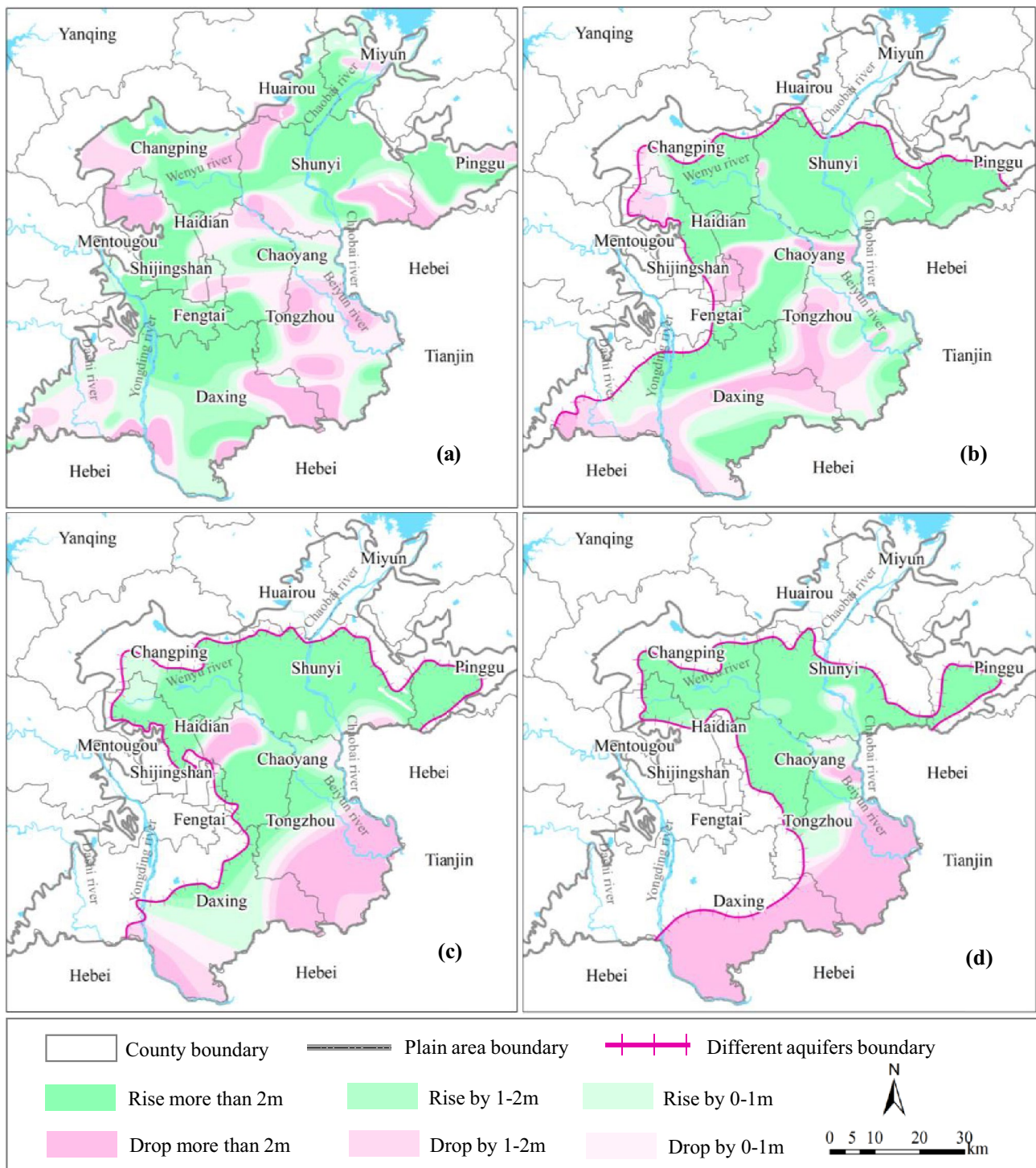


Fig. 8 Comparison of groundwater levels of different aquifer groups in 2015 and 2020

level change curves of 4 monitoring wells in the southeast of Tongzhou are shown in Fig. 9d. From 2010 to 2020, the middle-deep and deep confined water levels continued to decline. An average annual decline was 1.18–1.75 m, and the largest cumulative decline 19.28 m.

Change of land subsidence

The time series information of land subsidence in Beijing Plain from 2013 to 2020 is obtained in this paper by means of PSI technique (Fig. 10). Chaoyang and part of Tongzhou,

Table 3 Calibration of the displacements measured by PSI using levelling records

Benchmark number	Average vertical movement by PSI (mm/year)	Average vertical movement by levelling (mm/year)	Difference (mm/year)	Benchmark number	Average vertical movement by PSI (mm/year)	Average vertical movement by levelling (mm/year)	Difference (mm/year)
S01	-42.5	-38.4	-4.1	S16	-6.9	-10.2	3.3
S02	-38.0	-32.0	-6.0	S17	-26.0	-27.5	1.5
S03	-39.2	-42.9	3.7	S18	-6.2	-3.5	-2.7
S04	-18.0	-21.0	3.0	S19	-18.5	-16.2	-2.3
S05	-19.8	-25.2	5.4	S20	-36.4	-31.0	-5.4
S06	-32.2	-37.8	5.6	S21	-25.6	-18.3	-7.3
S07	-40.1	-46.7	6.6	S22	-18.3	-15.2	-3.1
S08	-15.3	-18.3	3.0	S23	2.2	-1.1	3.3
S09	-10.2	-6.0	-4.2	S24	-45.0	-52.2	7.2
S10	3.5	-4.8	8.3	S25	2.1	-1.6	3.7
S11	-134.0	-126.9	-7.1	S26	-32.5	-25.1	-7.4
S12	-26.0	-34.0	8.0	S27	-5.4	-9.7	4.3
S13	-5.8	-11.6	5.8	S28	-24.0	-20.0	-4.0
S14	-19.8	-16.3	-3.5	S29	-29.0	-31.4	2.4
S15	-28.9	-33.2	4.3	S30	-135.3	-129.2	-6.1

Mean square error (mm/year) 5.16

which are situated in the east of the Beijing Plain, are the most serious land subsidence development areas. Several major land subsidence centers are connected together, and the subsidence center velocity has been above 100 mm/year for many years. The distribution of land subsidence in the northern part of the plain was scattered, and the areas with severe subsidence were mainly distributed in the northern part of Haidian, in the southern part of Changping and part of Shunyi. The time series information of land subsidence show that since the operation of SNWDP-CR at the end of 2014, the land subsidence in Beijing has gradually slowed down. The land subsidence in the northern part of the plain slowed down in 2016, and the area of the subsidence gradually decreased. The land subsidence in the eastern part of the plain mainly slowed down in 2018 Table 5.

From 2013 to 2020, the average land subsidence rate decreased from 21.7 mm/year in 2013 to 10.85 mm/year in 2020, with a decrease of 10.85 mm/year (Fig. 11a). The area of severe subsidence (subsidence rate greater than 50 mm/year) decreased from 572 km² in 2013 to 45 km² in 2020, with a decrease of 527 km² (Fig. 11a). The total volume of land subsidence reduced from 13,210×10⁴ m³ in 2013 to 5338×10⁴ m³ in 2020, with a decrease of 8120×10⁴ m³ (Fig. 11b).

From the perspective of the vertical distribution of land subsidence, the main subsidence layers of the Beijing Plain are currently concentrated in the second and third compression layer groups, with average subsidence accounting for 34.11% and 57.36% (Table 6). By comparing the annual subsidence of each monitoring station in 2014 and in 2020, it can be found that, except for the increase in the annual subsidence of the Yufa extensometer, the annual subsidence

of the extensometers of the other stations decreased significantly. The land subsidence of the extensometer in Zhangjiawan station decreased most, with a decrease of 73.12 mm. As for the groundwater level corresponding to the main subsidence layer, except for Zhangjiawan and Yufa stations, the groundwater levels of the other stations all rose. Among them, the groundwater level of Yufa station declined significantly, especially the deep confined water D7-2 (monitoring depth: 132–169 m) and D7-1 (monitoring depth: 207–295 m), the water level decline of which was 2.76 m and 3.11 m, respectively (Table 7).

Through the analysis above, it can be found that since the water from SNWDP-CR entered Beijing in December 2014, the water shortage of Beijing has been alleviated, and the groundwater level in most areas has risen significantly, and the corresponding land subsidence has gradually slowed down. On the whole, the groundwater level in the northern part of the plain had gradually risen since 2015, and land subsidence had gradually decreased since 2016. The groundwater level in the eastern part of the plain began to rise gradually around 2017, and the land subsidence had been significantly decreased since 2018. This is mainly due to the hysteresis in the water release and compression of the cohesive soil layer, and the slowdown of land subsidence will lag behind the rise of the groundwater level for a period of time (Zhang et al. 2007, 2012; Shi et al. 2008; Ye et al. 2016a). However, in the southeastern and southern parts of the plains, groundwater is still over-exploited and the middle-deep and deep confined water levels continue to decline, resulting in continued development of land subsidence in these areas.

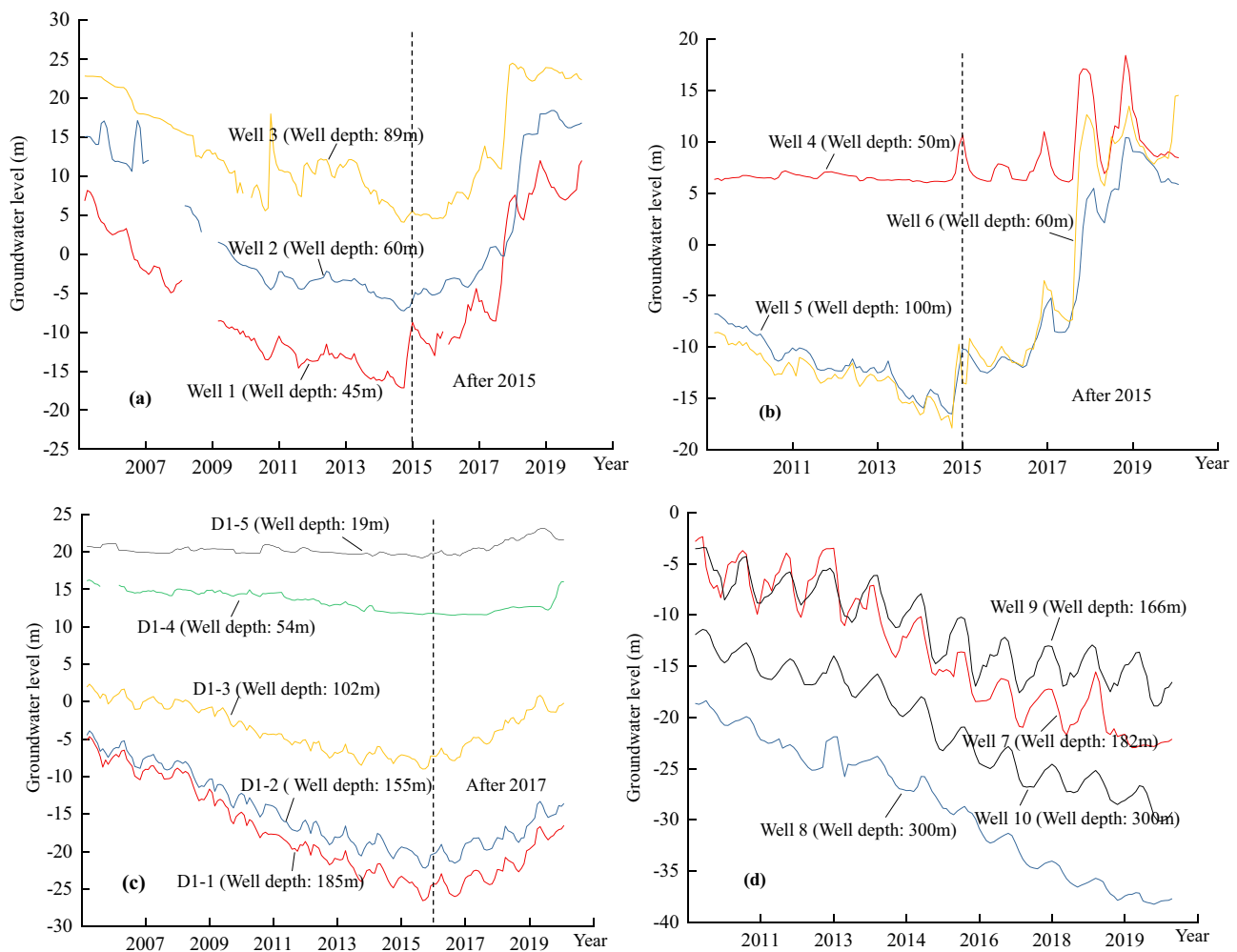


Fig. 9 Groundwater level change curves in the typical areas. **a** The groundwater level change curves of Well-1, Well-2, and Well-3, which are located in the northern part of the plain. **b** The groundwater level change curves of Well-4, Well-5, and Well-6, which are located near the channel of Chaobai River in the northern part of

the plain. **c** The groundwater level change curves of D1-1, D1-2, D-3, D-4, and D1-5 wells, which are located in the Wangsiying land subsidence monitoring station in the eastern part of the plain. **d** The groundwater level change curves of Well-7, Well-8, Well-9, and Well-10, which are located in the southeastern part of the plain

Deformation characteristics of soil layers

Since the change form of the groundwater level in the soil layer reflects the change process of the effective stress, it will directly affect the deformation behavior of the soil layer (Shi et al. 2008; Zhang et al. 2015). Therefore, after the operation of the SNWDP-CR, the aquifer and its corresponding compression layer will also show different deformation characteristics when the groundwater level changes from falling to rising in the plain. In this paper, the extensometer and groundwater level observation data of 7 land subsidence monitoring stations are used to study the deformation characteristics of soil layers with different lithologies and different depths before and after the SNWDP-CR operation. The representative soil layer deformation characteristics are selected for analysis, and the soil layers with similar

characteristics are grouped. Since the unconfined water is easily affected by many external factors, the first compression layer groups are characteristic of complex deformation. At the same time, the subsidence of the second and third compression layer groups accounts for about 92% of the total subsidence, and they are the main subsidence layers (Table 6). Therefore, the deformation characteristics of the second and third compression layer groups and sand layer are analyzed in the next paragraph. In Figs. 12–18, the negative value of the cumulative deformation represents soil compression, and the positive value rebound.

Sand layers

The monitoring layer of extensometer F3-8 in Tianzhu Station is 49–65 m, with a total thickness of 16 m. It is a

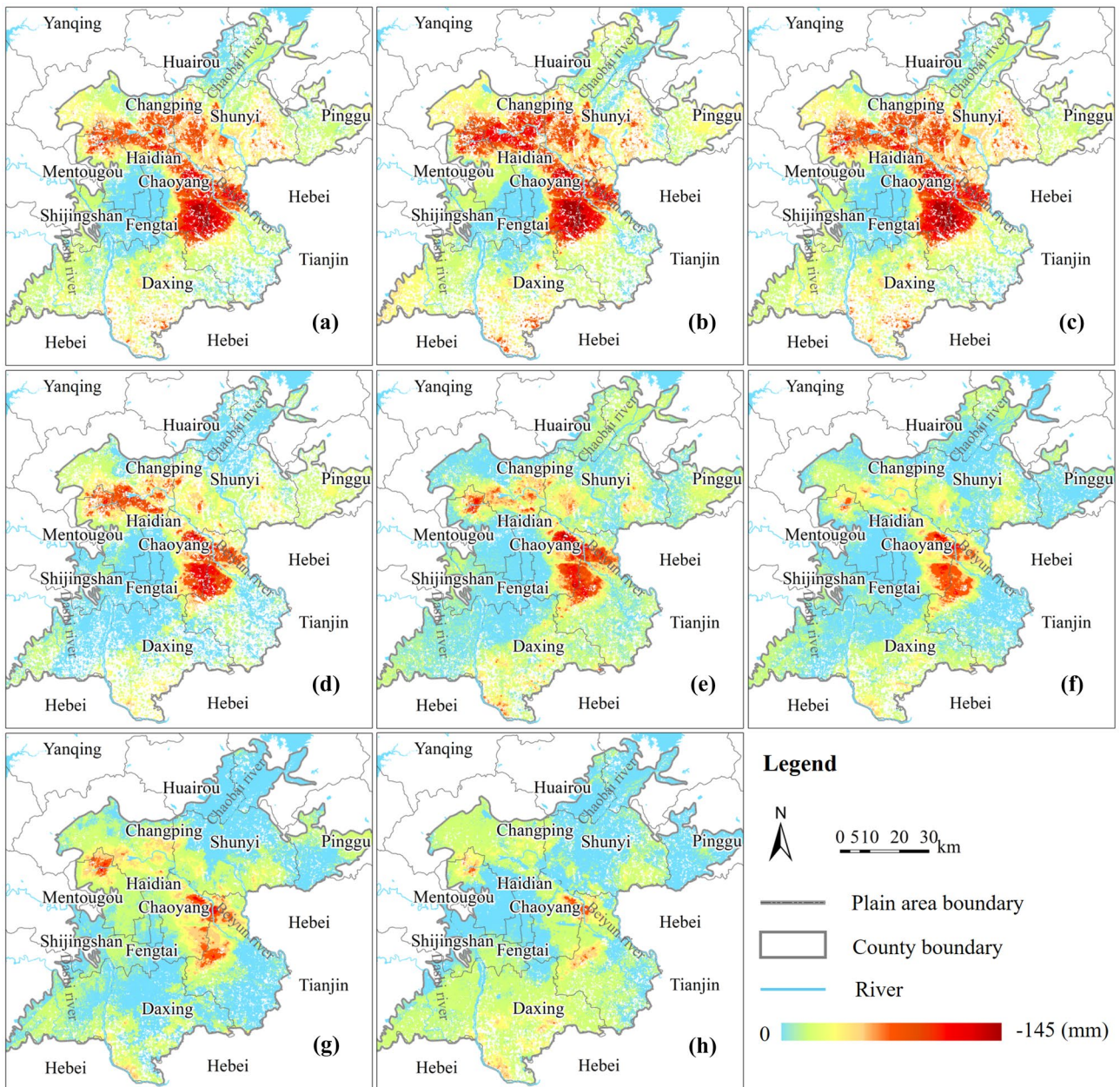


Fig. 10 The distribution characteristics of land subsidence in Beijing Plain (2013–2020). **a** 2013, **b** 2014, **c** 2015, **d** 2016, **e** 2017, **f** 2018, **g** 2019, **h** 2020

Table 4 Comparison of groundwater level changes in different aquifers in 2015 and 2020

Aquifers	Rising area of groundwater level (km ²)	Falling area of groundwater (km ²)	Average rising range of groundwater level (m)
Unconfined aquifer	3645	2412	2.72
First confined aquifer	3086	1470	3.68
Second confined aquifer	2488	1296	3.31
Third confined aquifer	1703	1170	1.91

Table 5 Statistics on the proportion of subsidence in each compression layer group of land subsidence monitoring stations

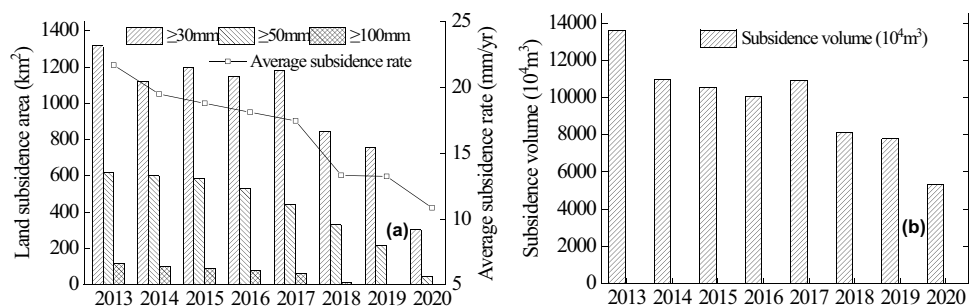
Compression layer group		Tianzhu	Baxianzhuang	Wangsiying	Zhang Jiawan	Wang Jing	Pingzhuang	Yufa	Average percentage
First compression layer group	Monitoring depth (m)	2–35	2–59	2–24	2–49	2–29	2–32	2–53	8.53%
	Percentage of subsidence	2.49%	11.06%	2.71%	9.21%	1.53%	5.27%	27.42%	
Second compression layer group	Monitoring depth (m)	35–149	59–144	24–94	49–126	29–99	32–120	53–116	34.11%
	Percentage of subsidence	62.23%	55.59%	28.09%	-3.78%	30.81%	22.56%	19.76%	
Third compression layer group	Monitoring depth (m)	Below 149	Below 144	94–182	Below 126	Below 99	Below 120	Below 116	57.36%
	Percentage of subsidence	35.28%	33.35%	69.20%	94.57%	67.67%	72.17%	52.81%	

confined aquifer which is mainly composed of fine sand and medium-coarse sand and whose top is covered with a 2 m thick clay layer. It can be seen from Fig. 12a that from 2006 to 2016, the average annual water level showed an overall downward trend over time, and the annual water level was dominated by seasonal fluctuations. The average annual water level dropped from -4.37 m in 2006 to -8.73 m in 2016, a drop of 4.36 m. The extensometer F3-8 compressed by 5.19 mm cumulatively. From 2017, the groundwater level began to gradually rise. By the end of 2020, the average annual water level rose to -3.00 m, an increase of 5.73 m. The extensometer F3-8 rebounded by 1.94 mm. From 2006 to 2016, the sand layer showed an almost synchronous compression-rebound as the groundwater level decreased or increased in an annual cycle. After 2017, when the groundwater level changed from fall to rise, there was a slight hysteresis in the deformation of the sand layer. It can be seen from Fig. 12b that from 2006 to 2016 the loading and unloading curves of the sand layer under slow cyclic loading were very close, showing basically synchronous elastic deformation. After 2017, the groundwater level began to rise, but the sand layer did not rebound immediately, there being a hysteresis in deformation. This may be related to the creep deformation of the clay layer which covers the top of the sand layer.

Second compression layer group

The monitoring layer of extensometer F3-5 in Tianzhu Station is 102–117 m, with a total thickness of 15 m. The lithology is mainly cohesive soil with a 2-m-thick fine sand layer in between. As shown in Fig. 13a, from 2006 to 2016, the groundwater level showed an overall downward trend, and the water level rose at the end of 2017. Before 2017, the groundwater level cyclically reciprocated. In each cycle, the water level fell more than it rose. Correspondingly, the soil layer bore the effects of loading and unloading, and each increase in stress was greater than the decrease in unloading, which means that the effective stress that the soil layer bore on the whole continued to increase. The soil layer was continuously compressed at a rate of about 10.3 mm/year. After 2017, although the groundwater level began to rise, the soil layer continued to compress, but the compression rate has slowed down. It can be seen from Fig. 13b that with the continual drop of the groundwater level, the compression curve developed toward the lower right, and the soil layer was rapidly compressed. Meanwhile, the soil layer showed plastic deformation, with the residual deformation relatively large. When the groundwater level rose, the soil layer still continued to compress, there being a hysteresis in deformation. This shows that this section of the soil layer did not

Fig. 11 Statistics maps of average subsidence rate, subsidence area and volume (2013–2020). **a** Statistics of average land subsidence rate and subsidence area from 2013 to 2020. **b** Statistics of land subsidence volume from 2013 to 2020



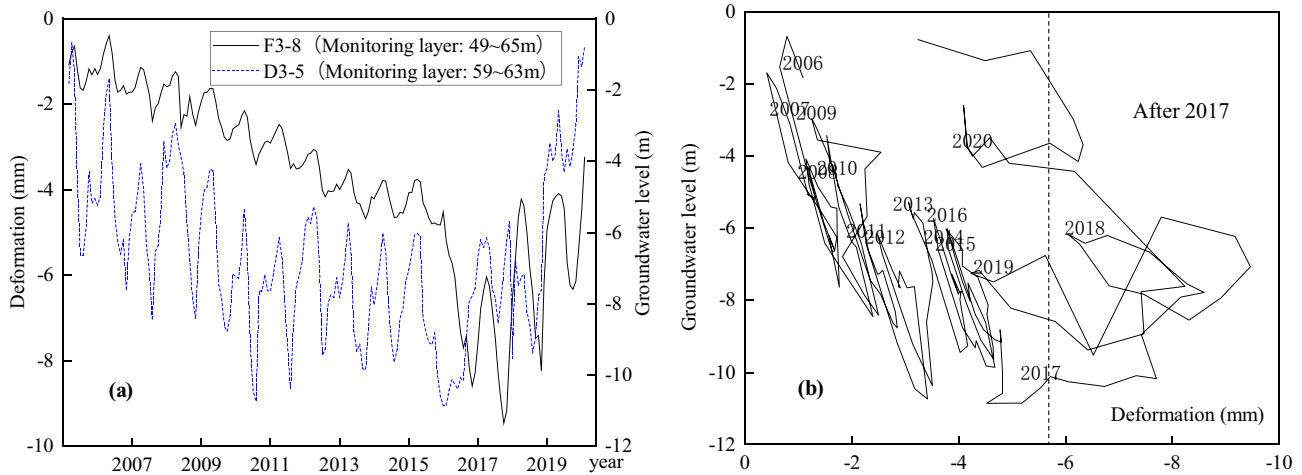


Fig. 12 Relationship between cumulative deformation of sand layer with groundwater level at F3-8 of Tianzhu station. **a** Time series curve of relationship between groundwater level and cumulative

deformation. **b** Relationship curve between groundwater level and cumulative deformation

only have plastic deformation with large residual deformation, but also contained creep deformation which related to the time development. It can be concluded that with the change of the groundwater level, the soil layer exhibits the characteristics of viscoplastic deformation.

The monitoring layer of extensometer F1-3 in Wangsiying Station is 66–94 m, with a total thickness of 28 m. It is mainly composed of clay layer and sand layer. The sand layer accounts for about 74% of the total thickness of the section, and the clay layer 26%. As shown in Fig. 14a, from 2006 to 2016, the groundwater level showed an overall downward trend. The average annual water level dropped from 1.97 m in 2006 to -7.32 m in 2016, with a drop amount of 9.29 m.

The extensometer F1-3 compressed by 81.40 mm cumulatively. Since 2017, the groundwater level has risen significantly. By the end of 2019, the average annual water level had risen to -1.03 m, with an increase amount of 6.29 m. Correspondingly, the compression rate of the extensometer F1-3 slowed down to some degree, and there was a slight rebound in 2019. As shown in Fig. 14b, the monitoring layer was dominated by sand. From 2006 to 2016, with the decline of the groundwater level, the soil layer continued to compress rapidly, with a large amount of plastic deformation and with the phenomenon of hysteresis. This was related to the fact that the dissipation of excess pore water pressure in the soil layer lagged behind the change of the aquifer

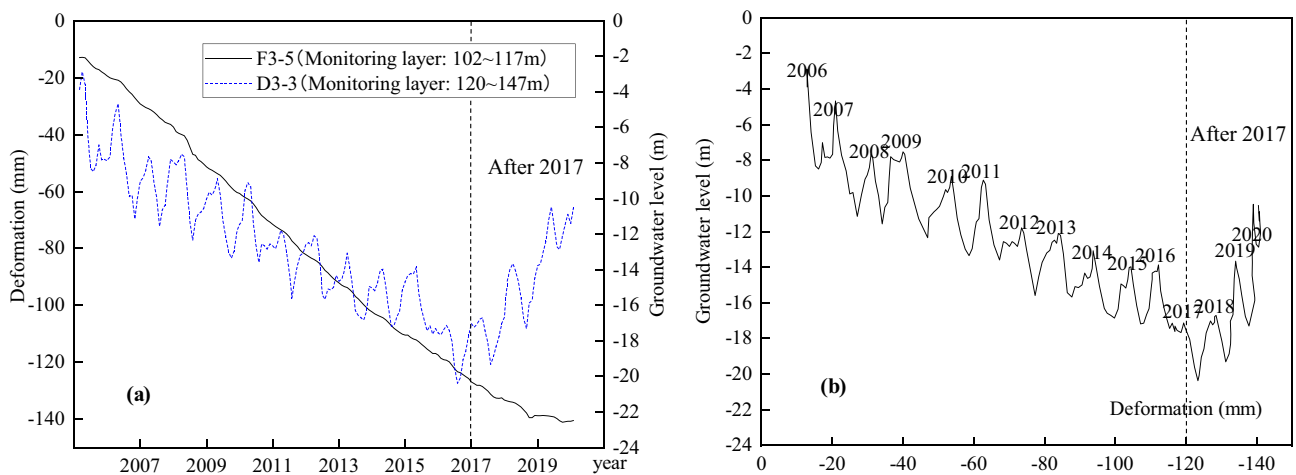


Fig. 13 Relationship between cumulative deformation of soil layer with groundwater level at F3-5 of Tianzhu station. **a** Time series curve of relationship between groundwater level and cumulative

deformation. **b** Relationship curve between groundwater level and cumulative deformation

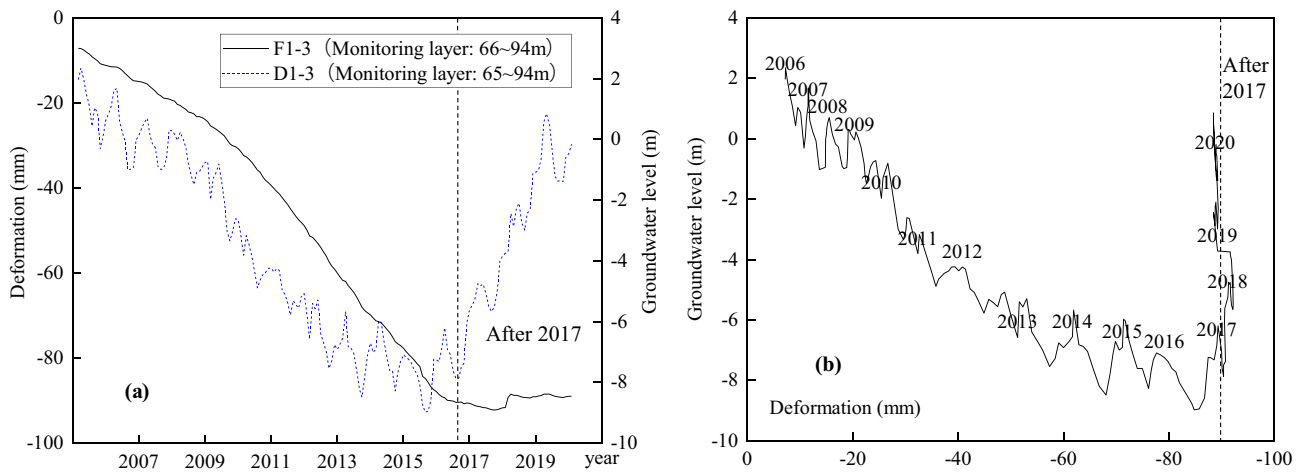


Fig. 14 Relationship between cumulative deformation of soil layer with groundwater level at F1-3 of Wangsiying station. **a** Time series curve of relationship between groundwater level and cumulative

deformation. **b** Relationship curve between groundwater level and cumulative deformation

water level, and it may also be related to the creep deformation. After 2017, when the local water level has risen significantly, the compression rate of the soil layer has slowed down, including plastic and creep deformation. There were elastic deformation occurred in 2019 and 2020. It can be seen that with the change of the groundwater level, the soil layer undergoes a process of changing from viscoplastic deformation to viscoelastic plastic one.

Third compression layer group

The monitoring layer of extensometer F1-2 in Wangsiying Station is 94–148 m, with a total thickness of 54 m. It is mainly composed of cohesive soil layer and sand layer,

and the cohesive soil layer accounts for about 77% of the total thickness of this section. As shown in Fig. 15a, from 2006 to 2016, the groundwater level showed a downward trend year by year. The average annual water level dropped from -5.80 m in 2006 to -20.76 m in 2016, with a drop amount of 14.96 m. The extensometer F1-3 compressed by 241.10 mm cumulatively. Since 2017, the groundwater level has risen significantly. By the end of 2020, the average annual water level had risen to -14.46 m, with an increase amount of 6.30 m. The compression rate of extensometer F1-2 slowed down to some degree. As shown in Fig. 15b, the groundwater level continued to drop, and the soil layer was compressed rapidly, with the amount of plastic deformation large. When the groundwater level rose, the soil layer

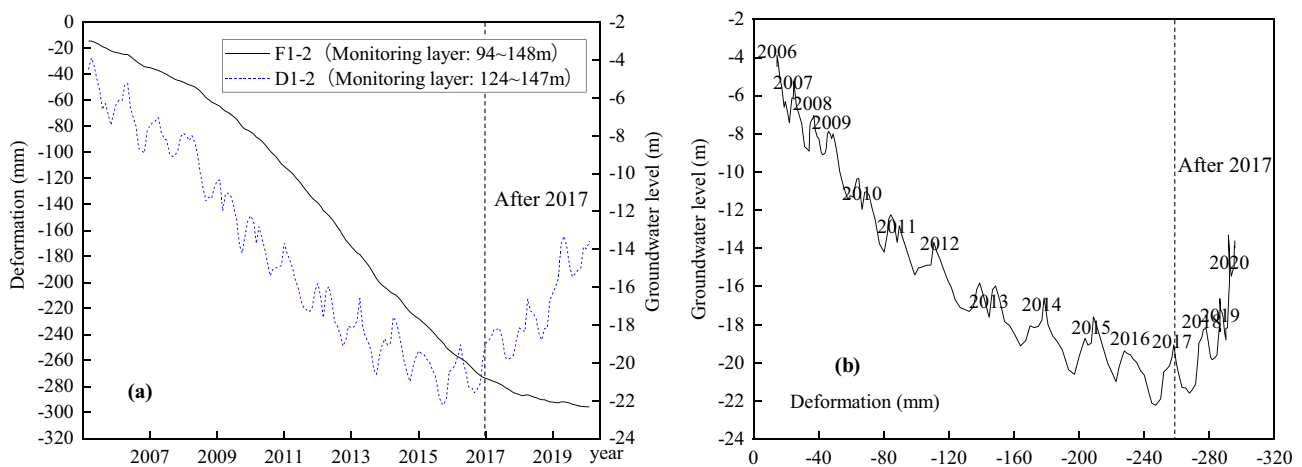


Fig. 15 Relationship between cumulative deformation of soil layer with groundwater level at F1-2 of Wangsiying station. **a** Time series curve of relationship between groundwater level and cumulative

deformation. **b** Relationship curve between groundwater level and cumulative deformation

Table 6 The subsidence of each monitoring station and the main compression layer correspond to the change of groundwater level in 2014 and 2020

Year	Wangsiying	Wang Jing	Tianzhu	Baxianzhuang	Pingzhuang	Zhang Jiawan	Yufa
Subsidence (mm)	2014 63.69	42.99	39.48	28.36	19.86	93.23	31.82
	2020 4.34	13.40	1.08	12.21	7.03	20.11	32.85
Average groundwater level corresponding to the second compression layer group (m)	2014 D1-4	12.76	D3-4	D4-5	D5-4	D6-4	D7-4
	D1-3	-7.14	D3-3	D4-4	D5-3	D6-3	D7-3
	D1-4	13.40	D3-4	D4-5	D5-4	D6-4	D7-4
	D1-3	-0.50	D3-3	D4-4	D5-3	D6-3	D7-3
	D1-2	-18.84	D3-2	D4-3	D5-2	D6-2	D7-2
Average groundwater level corresponding to the third compression layer group (m)	2014 D1-1	-22.29	D3-1	D4-2	D5-1	D6-1	D7-1
	D1-2	-14.53	D3-2	D4-3	D5-2	D6-2	D7-2
	D1-1	-17.61	D3-1	D4-2	D5-1	D6-1	D7-1
		0.50	D3-1	D4-2	D5-1	D6-1	D7-1

Table 7 Deformation characteristics of different compression layer groups and sand layers before and after SNWDP-CR operation under different water level change modes

Compression layer groups	Patterns of groundwater level changes	Deformation characteristics of soil layers before 2017	Deformation characteristics of soil layers after 2017
Second compression layer groups (middle and deep soil layers)	The groundwater level continued to decline at a relatively rapid rate and then gradually rose	(I) The stage of the groundwater level continued to decline: the soil layer was compressed rapidly, with the residual deformation large. The soil layer was mainly plastic deformation, creep deformation included	The stage of the groundwater level continued to rise: (II) when the soil layer was dominated by cohesive soil, the soil layer continued to compress, and the compression speed slowed down. The soil layer contained plastic deformation and creep deformation. (III) When the soil layer was dominated by sand, the compression rate of the soil layer is significantly slowed down. The soil layer contained plastic deformation, creep deformation and elastic deformation
Third compression layer groups (deep soil layers)			
Sand layers	The groundwater level declined slightly first, then gradually rose	(IV) The soil layer was mainly elastic deformation, with the residual deformation very small	

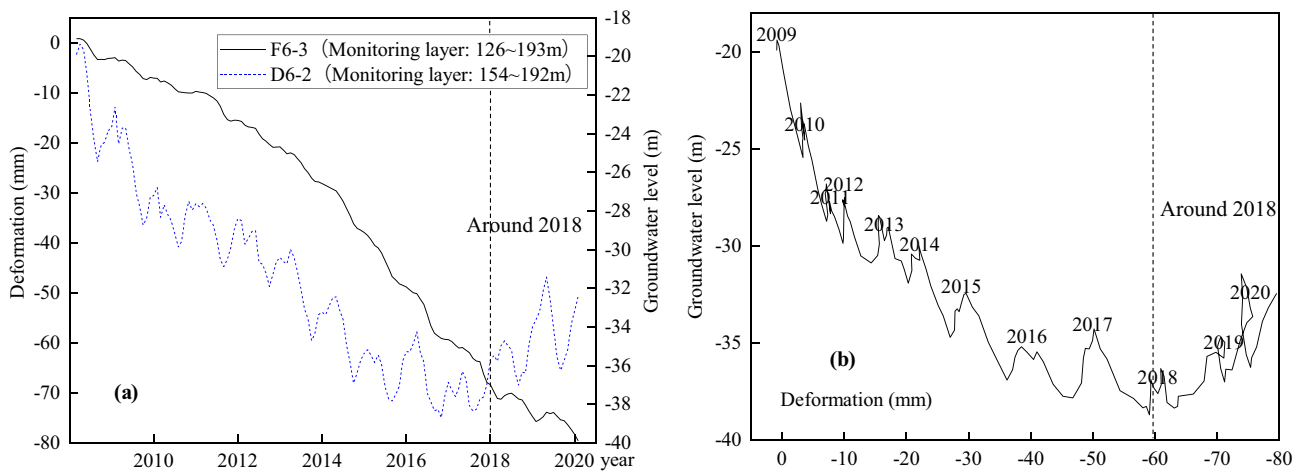


Fig. 16 Relationship between cumulative deformation of soil layer with groundwater level at F6-3 of Zhangjiawan station. **a** Time series curve of relationship between groundwater level and cumulative

deformation. **b** Relationship curve between groundwater level and cumulative deformation

continued to compress, there being a hysteresis in deformation. This shows that there was not only plastic deformation with large residual deformation, but also creep deformation which related to the time development. It can be found that with the change of the groundwater level, the soil layer exhibits the characteristics of viscoplastic deformation.

The monitoring layer of extensometer F6-3 in Zhangjiawan Station is 126–193 m, with a total thickness of 67 m. It is mainly composed of cohesive soil layer and sand layer. The cohesive soil layer accounts for about 52% of the total thickness of the section, and the sand layer 48%. As shown in Fig. 16a, from 2009 to 2017, the groundwater level showed an overall downward trend, and the groundwater level rose in 2018. Before 2018, with the decline of the groundwater level, the soil layer was compressed continuously. After 2018, the groundwater level rose, and the soil layer still compressed, but the compression rate slowed down. Meanwhile, there was a slight rebound in 2019 and 2020. As shown in Fig. 16b, the curve always developed toward the right with the continual decline of the groundwater level. There was very small rebound of the soil, or there was no rebound, and there was a hysteresis in the deformation of the soil. This shows that there was not only plastic deformation with large residual deformation, but also creep deformation in this section of the soil. After 2018, when the local water level rose, the curve still developed towards the right, there being plastic deformation and creep deformation. At the same time, there appeared a hysteresis loop in 2019 and 2020, indicating that there were still the characteristics of elastic deformation.

What has been discussed above is the typical deformation curves of long-term series of different depths and

lithological soil layers in different water level change modes in land subsidence monitoring stations. It can be found that most of the middle-deep and deep confined groundwater levels continued to decline before 2017 and gradually rose after 2017. Therefore, the year 2017 can be regarded as the time node. Under the comprehensive consideration of different groundwater level change modes, the deformation characteristics of different compression layer groups and sand layer can be summarized as shown in Table 8. The groundwater levels corresponding to the second and third compression layer groups continued to decline at a rapid rate before 2017 and then gradually rose after 2017. The second and third compression layer groups showed the (I) deformation type before 2017, and the different lithological soil layers showed the (II) and (III) deformation types after 2017. The groundwater level corresponding to the sand layer decreased slightly before 2017 and gradually rose after 2017. The sand layer showed the (IV) deformation type.

Geotechnical test of soil deformation

On the basis of obtaining the deformation characteristics of the soil layer, the loading, unloading, and repeated loading and unloading test methods are used to compare different lithological soil samples. The deformation characteristics and creep effects of different lithological soil layers under different loading and unloading modes are analyzed. In the test process above, each level of load is applied or removed instantaneously, to observe the stability of the deformation under each level of load, and the deformation less than 0.005 mm/h is regarded as the stability standard (Zhang et al. 2012, 2016). The location of the soil sample is shown

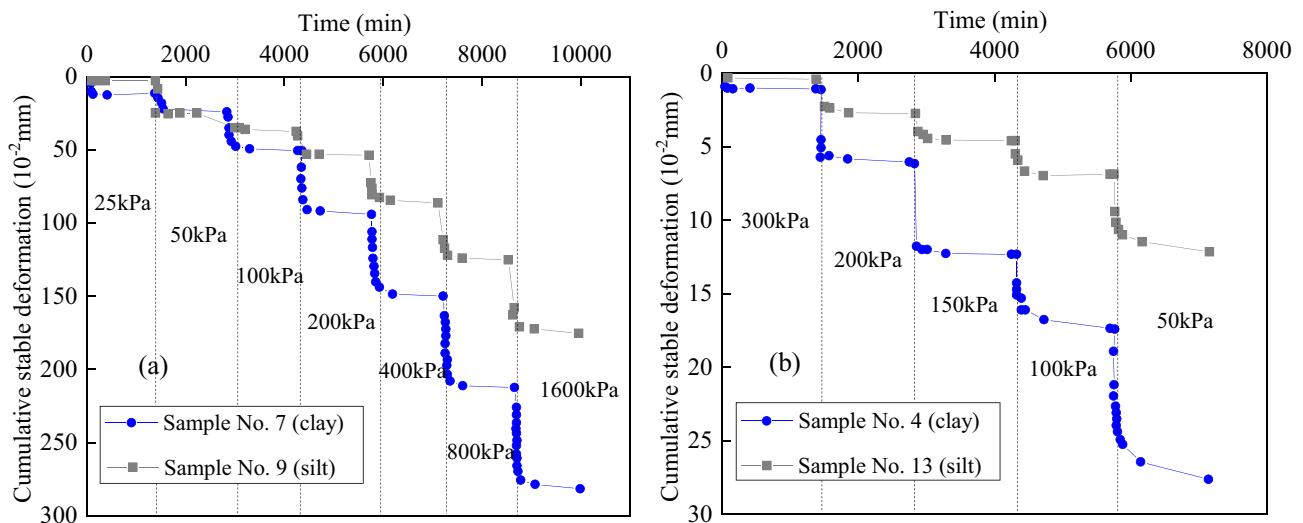


Fig. 17 Cumulative deformation curve of loading and unloading of clay and silt. **a** Cumulative deformation curve of loading of clay and silt. **b** Cumulative rebound curve of unloading step by step of clay and silt after reaching stable deformation from 400 kPa

in Fig. 1. The physical and mechanical properties of the soil sample are shown in Table 9.

It can be seen from Fig. 17a that firstly, after each level of pressure is loaded, the deformation of the soil sample is basically stable after about 120 min; secondly, the total deformation of the clay sample and the silt sample is 2.822 mm and 1.0 mm, respectively. Under the same load condition, the deformation of clay is greater than that of silt. As the pressure increases, the difference in the amount of deformation becomes larger and larger. It can be seen from Fig. 17b as follows: Firstly, after the soil sample is loaded with 400 kPa and reaches the stable deformation, with the gradual unloading, the total rebound of the clay sample and the silt sample is 0.277 mm and 0.121 mm. The rebound of clay is more than the silt obviously under the same load. Secondly, since the unloading of the soil sample is completed instantaneously, the instantaneous rebound of the soil sample is very obvious after each level of unloading. With the progress of the test, when the effective stress gradually approaches the load borne by the soil, the rebound amount of the soil sample gradually decreases and tends to a constant value. Thirdly, the smaller the unloading pressure of the soil sample is, the longer time will be taken for the soil sample to complete the rebound and achieve stable deformation.

Repeated loading and unloading tests are carried out on No. 6, No. 16, and No. 21 soil samples to simulate the deformation characteristics of soil layer during the rise and decline of groundwater level. It can be seen from Fig. 18 is as follows: Firstly, the deformation of the clay in the first loading and unloading is greater than

the second, and the deformation of the latter two loading and unloading gradually increases and is greater than the first loading and unloading. The main reason is the large porosity of the clay. During the first loading and unloading, the soil sample is pressurized and drained, easy to compress and deform greatly. During the second loading and unloading, however, because the load of the soil sample is still small and it has already gone through one loading and unloading cycle, the soil sample's creep increases, and the amount of deformation is small. The loads of the third and fourth cycles are larger, and the creep amount of the soil sample becomes larger and larger until the soil sample is destroyed. So there is a large amount of deformation. Secondly, the deformation of silty clay and silty soil in each loading, and unloading cycle is greater than the previous cycle. This is mainly because after the porosity of the soil sample reduces, the soil sample is not easy to be compressed, and it is easy to reach a consolidated state, and the amount of creep is small. When the maximum load gradually increases, the amount of deformation also gradually increases. Thirdly, the time effect of creep is as follows: clay > silty clay > silt. It shows that the larger porosity, the more creep deformation is likely to occur.

Change of elastic and inelastic skeletal specific storage rate

According to the above-mentioned deformation characteristics of soil layers with different lithologies and different depths, the elastic and inelastic skeletal specific storage

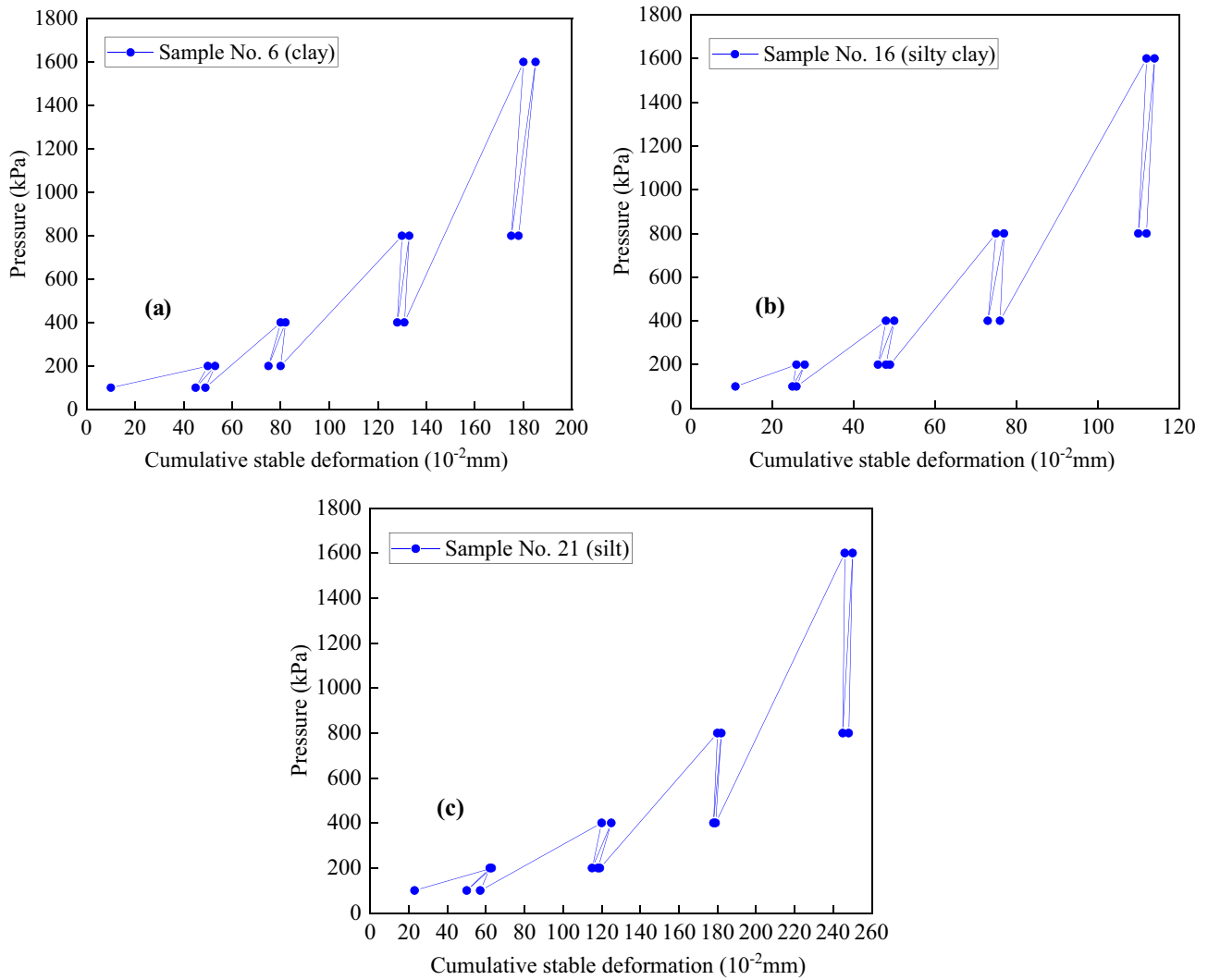


Fig. 18 Cumulative deformation curves of soil samples with different lithologies after repeated loading and unloading. **a** Cumulative deformation curve of No. 6 clay sample after repeated loading and unloading.

b Cumulative deformation curve of No. 16 silty clay after repeated loading and unloading. **c** Cumulative deformation curve of No. 21 silt soil after repeated loading and unloading

rates of the sand layer and compressed layer group can be calculated. The average of the results is shown in Table 10. In terms of the results of Galloway and Burbey (2011) when the value of S_{ske} is 5×10^{-4} , it is a typical elastic

skeletal specific storage coefficient. When the value of S_{skv} is 5×10^{-3} , it is likely to be an inelastic skeletal specific storage rate coefficient during land subsidence. Of course, when the water storage rate is calculated, the water storage

Table 8 Statistics of physical and mechanical properties of soil samples

Sample number	Lithology	$\omega(\%)$	$\gamma(g/cm^3)$	Δs	e_0	$E_{s1-2}(MPa)$	$a_{v1-2}(MPa^{-1})$	c_c/c_s	$P_c(kPa)$
4	Clay	37.340	1.763	2.74	1.134	2.291	0.900	0.150	1217
6	Clay	23.825	1.826	2.74	0.858	9.634	0.192	0.064	1870
7	Clay	22.257	2.007	2.74	0.669	4.356	0.372	0.124	1223
9	Silt	22.167	2.016	2.69	0.631	10.454	0.153	0.051	1276
13	Silt	17.870	1.799	2.69	0.487	18.573	0.078	0.013	1128
16	Silty clay	18.985	2.087	2.72	0.551	11.021	0.140	0.046	1058
21	Silt	20.981	1.991	2.69	0.634	4.879	0.331	0.110	1597

Table 9 Elastic and inelastic skeletal specific storage rate of compressed layer group and sand layer

Compression layer groups	Extensometers and wells	Time interval	S_{skv} (m^{-1})	Time interval	S_{ske} (m^{-1})
Second compression layer groups	F3-5, D3-3	2006.1 ~ 2016.12	5.11×10^{-4}	—	—
		2017.1 ~ 2020.12	2.10×10^{-4}	—	—
Third compression layer groups	F1-3, D1-3	2006.1 ~ 2016.12	3.13×10^{-4}	2017.1 ~ 2020.12	6.03×10^{-7}
		2017.1 ~ 2020.12	2.88×10^{-4}		
	F1-2, D1-2	2006.1 ~ 2016.12	2.88×10^{-4}	—	—
		2017.1 ~ 2020.12	1.18×10^{-4}	—	—
F6-3, D6-2	2009.1 ~ 2016.12	4.88×10^{-5}	—	—	
	2017.1 ~ 2020.12	1.82×10^{-4}	—	—	
Sand layers	F3-8, D3-5	—	—	2006.1 ~ 2016.12	2.84×10^{-5}
		—	—	2017.1 ~ 2020.12	1.49×10^{-5}

coefficient needs to be divided by the initial thickness of the soil layer. At the same time, Hoffmann et al. point out that for aquifers dominated by loose clay and mucky, the value of S_{skv} is usually tens to hundreds of times larger than that of S_{ske} . It can be seen from Table 10 that the inelastic skeletal specific storage rate in different compression layer groups is 1 to 2 orders of magnitude larger than the elastic skeletal specific storage rate. It shows that when the soil layer is mainly cohesive soil, with the rise of the water level, the soil layer will still have a large residual deformation and will continue to compress without rebound or with small rebound. The F3-5 in the second compression layer group, and the F1-2 and F6-3 in the third compression layer group all show larger residual deformation. It is noticeable that the inelastic skeletal specific storage rate of F6-3 from 2009 to 2016 is 4.88×10^{-5} , which is small and close to the elastic skeletal specific storage rate. The reason is that the water-bearing sand layer accounts for 48% of the total thickness of this section, which has a certain influence on the inelastic deformation of the soil layer. Since the inelastic skeletal specific storage rate is greater than the elastic skeletal specific storage rate, there will be residual deformation when the water level is restored (Ye et al. 2016a, b).

It is noticeable that as for different stages of the soil deformation, the change in water storage rate is not constant, and its value depends on the relationship between the effective stress and the preconsolidation pressure (Hoffmann et al. 2003; Liu and Helm 2008a, b). For example, the extensometer F1-3 with the year 2017 taken as the time nodes, the soil layer changed from plastic deformation to elastic deformation. The water storage rate also changed from inelastic skeletal specific storage rate to elastic skeletal specific storage rate. The rest of the extensometers took the year 2017 as the time node, and the soil water storage rate in different periods also showed different characteristics of change. This further illustrates that after the operation of SNWDP-CR, the deformation characteristics of different lithologies and

depths of soil layers have changed, and the corresponding hydrogeological parameters have also changed greatly. Therefore, in order to simulate the land subsidence under the new situation where the groundwater level continues to rise after the operation of the SNWDP-CR, suitable soil constitutive relations and corresponding hydrogeological parameters must be selected according to the deformation characteristics of the soil.

Conclusions

This study has investigated the impact of the 6 years of SNWDP-CR operation on the groundwater and land subsidence in the Beijing Plain. PSI, GIS spatial analysis, stress–strain analysis, mathematical statistics, and geotechnical tests are used for the first time to analyze the changes of the groundwater flow field, groundwater level, land subsidence, soil deformation, and hydrogeology parameters before and after the SNWDP-CR operation. The research results are of great significance for the further determination of the constitutive relationship of soil layer deformation before and after the SNWDP-CR operation and the establishment of an appropriate coupling model of groundwater and land subsidence.

Affected by various measures such as SNWDP-CR, reduction of groundwater exploitation, shut-down of wells, and recharge of aquifers, the groundwater level of the first to fourth aquifer groups in most areas of the Beijing Plain rose significantly from 2015 to 2020, and the corresponding land subsidence has gradually slowed down. The average groundwater level of the four aquifer groups rose by 2.72 m, 3.68 m, 3.31 m, and 1.91 m, respectively. The average land subsidence rate decreased from 18.8 mm/year in 2015 to 10.85 mm/year in 2020, with a decrease of 7.95 mm/year. However, the groundwater level in some areas is still declining, and land subsidence continues to develop.

The main subsidence layers of the Beijing Plain are currently concentrated in the second and third compression layer groups, with average subsidence accounting for 34.11% and 57.36%. Since the operation of SNWDP-CR, except for the increase in the annual subsidence of the Yufa extensometer, the annual subsidence of the extensometers of the other stations decreased significantly. As for the groundwater level corresponding to the main subsidence layer, except for Zhangjiawan and Yufa stations, the groundwater levels of the other stations all rose.

The deformation characteristics of different lithological soil layers under different water level change modes can be summarized into 4 categories before and after the SNWDP-CR operation. The sand layer is mainly characteristic of elastic deformation. The soil deformation characteristics of the second and third compression layer groups are quite different when the groundwater level changes from declining to rising. When the soil layer is dominated by cohesive soil, it always exhibits plastic and creep deformation. If the sand layer is the main one, the soil layer exhibits plastic and creep deformation in the stage of groundwater level decline, and plastic, creep, and elastic deformation in the stage of water level rises.

Under the condition of gradual loading, the deformation of clay was greater than that of silt. With the increase of the pressure, the difference in the amount of deformation increased. Under the condition of gradual unloading, the rebound amount of clay was greater than that of silt. And the rebound amount gradually decreased until it tended to a constant value. Under the condition of repeated loading and unloading, silty clay and silt soil were easier to consolidate than clay, and the amount of creep was smaller. The time effect of creep was as follows: clay > silty clay > silt. It shows that the larger porosity, the more creep deformation is likely to occur.

After the operation of SNWDP-CR, the hydrogeological parameters corresponding to different lithology and soil layers of different depths changed greatly. The change in the elastic and inelastic skeletal specific storage rate of the sand layer and compressed layer group were not constant, but changed with the different deformation characteristics of the soil layer. The inelastic skeletal specific storage rate of different compression layer groups was 1 to 2 orders of magnitude larger than the elastic skeletal specific storage rate. As the groundwater level decreases, the soil skeletal specific storage rate shows a decreasing trend.

Acknowledgements We greatly thank the editors, as well as the anonymous reviewers for their helpful or valuable comments on the paper.

Author contribution Kunchao Lei: Conceptualization, Methodology, Writing—original draft, Funding acquisition. Fengshan Ma: Conceptualization, Methodology, Funding acquisition, Supervision, Writing—review & editing. Beibei Chen: Conceptualization, Data curation, Formal analysis, Funding acquisition. Yong Luo: Data curation, Investigation, Project administration, Supervision. Wenjun Cui: Data curation, Project

administration, Supervision. Long Zhao: Investigation, Validation. Xinhui Wang: Investigation, Software. Aihua Sun: Investigation, Validation.

Funding This research is supported by the Natural Science Foundation of Beijing (Grant No. 8212042), Natural Science Foundation of China (Grant No. 41831293, 41771455), Beijing Outstanding Young Scientist Program (Grant No. BJJWZYJH01201910028032), and Beijing Youth Top Talent Project.

Data availability Data not available due to the Institute restrictions.

Declarations

Competing interests The authors declare no competing interests.

References

- Abidin H, Andreas H, Djaja R, Darmawan D, Gmal M (2008) Land subsidence characteristics of Jakarta between 1997 and 2005, as estimated using GPS surveys. *GPS Solutions* 12(1):23–32. <https://doi.org/10.1007/s10291-007-0061-0>
- Abidin H, Andreas H, Gumilar I, Fukuda Y, Pohan Y, Deguchi T (2011) Land subsidence of Jakarta (Indonesia) and its relation with urban development. *Natural Hazards* 59(3):1753–1771. <https://doi.org/10.1007/s11069-011-9866-9>
- Bai P, Liu C (2018) Evolution law and attribution analysis of water utilization structure in Beijing. *South-to-North Water Transf. Water Sci Technol* 16(4):6. <https://doi.org/10.13476/j.cnki.nsb-dqk.2018.0090>
- Cai X, Luan Y, Guo G, Liang Y (2009) 3D Quaternary geological structure of Beijing plain. *Geol in China* 36(5):1021–1029. <https://doi.org/10.3969/j.issn.1000-3657.2009.05.007>
- Cao A, Esteban M, Mino T (2020) Adapting wastewater treatment plants to sea level rise: learning from land subsidence in Tohoku. *Japan Natural Hazards* 103(7):885–902. <https://doi.org/10.1007/s11069-020-04017-5>
- Chaussard E, Burgmann R, Shirzaei M, Fielding EJ, Baker B (2014a) Predictability of hydraulic head changes and characterization of aquifer-system and fault properties from InSAR-derived ground deformation. *Journal of Geophysical Research: Solid Earth* 119(8):6572–6590. <https://doi.org/10.1002/2014JB011266>
- Chaussard E, Wdowinski S, Cabral-Cano E, Amelung F (2014b) Land subsidence in central Mexico detected by ALOS InSAR time-series. *Remote Sens Environ* 140:94–106. <https://doi.org/10.1016/j.rse.2013.08.038>
- Chen B, Gong H, Chen Y, Li X, Zhou C, Lei K, Zhu L, Duan L, Zhao X (2020) Land subsidence and its relation with groundwater aquifers in Beijing Plain of China. *Sci Total Environ* 735:139111. <https://doi.org/10.1016/j.scitotenv.2020.139111>
- Chen B, Gong H, Lei K, Li X, Zhou C, Gao ML, Guan HL, Lv W (2019) Land subsidence lagging quantification in the main exploration aquifer layers in Beijing plain. *China Int J Appl Earth Obs Geoinf* 75:54–67. <https://doi.org/10.1016/j.jag.2018.09.003>
- Du Z, Ge L, Ng AM, Lian X, Zhu Q, Horgan F, Zhang Q (2021) Analysis of the impact of the South-to-North water diversion project on water balance and land subsidence in Beijing, China between 2007 and 2020. *J Hydrol* 603(Pt. B). <https://doi.org/10.1016/j.jhydrol.2021.126990>
- Ferretti A, Prati C (2000) Nonlinear subsidence rate estimation using permanent scatterers in differential SAR interferometry. *IEEE Trans Geosci Remote Sens* 38(5):2202–2212. <https://doi.org/10.1109/36.868878>
- Ferretti A, Prati C, Rocca F (2001) Permanent scatterers in SAR interferometry. *IEEE Trans Geosci Remote Sens* 39(1):8–20. <https://doi.org/10.1109/36.898661>

- Galloway D, Burbey T (2011) Review: regional land subsidence accompanying groundwater extraction. *Hydrogeol J* 19(8):1459–1486. <https://doi.org/10.1007/s10040-011-0775-5>
- Galloway D, Hudnut K, Ingebritsen S, Phillips S, Peltzer G, Rogez F, Rosen P (1998) Detection of aquifer system compaction and land subsidence using interferometric synthetic aperture radar, Antelope Valley, Mojave Desert. *California Water Resour Res* 34(10):2573–2585. <https://doi.org/10.1029/98WR01285>
- Gambolati G, Teatini P (2015) Geomechanics of subsurface water withdrawal and injection. *Water Resour Res* 51(6):3922–3955. <https://doi.org/10.1002/2014wr016841>
- Gong H, Pan Y, Zheng L, Li X, Zhu L, Zhang C, Huang Z, Li Z, Wang H, Zhou C (2018) Long-term groundwater storage changes and land subsidence development in the North China Plain (1971–2015). *Hydrogeol J* 26:1417–1427. <https://doi.org/10.1007/s10040-018-1768-4>
- Guzy A, Malinowska A (2020) State of the art and recent advancements in the modelling of land subsidence induced by groundwater withdrawal. *Water* 12(7):2051–. <https://doi.org/10.3390/w12072051>
- Helm D (1975) One-dimensional simulation of aquifer system compaction near Pixley, California: 1. Constant Parameters *Water Resour Res* 11(3):465–478. <https://doi.org/10.1029/WR011i003p00465>
- HerreraGarcía G, Ezquerro P, Tomás R, BéjarPizarro M, López-Vinielles J, Rossi M, Mateos R, CarreónFreyre D, Lambert J, Teatini P, CabralCano E, Erkens G, Galloway D, Hung W, Kakar N, Sneed M, Tosi L, Wang H, Ye S (2021) Mapping the global threat of land subsidence. *J Sci (N.Y.)* 371(6524):34–36. <https://doi.org/10.1126/science.abb8549>
- Hoffmann J, Galloway D, Zebker H (2003) Inverse modeling of interbed storage parameters using land subsidence observations, Antelope Valley. *California Water Resour Res* 39:1031. <https://doi.org/10.1029/2001WR001252>
- Hoffmann J, Zebker H, Galloway D, Amelung F (2001) Seasonal subsidence and rebound in Las Vegas Valley, Nevada, observed by synthetic aperture radar interferometry. *Water Resour Res* 37(6):1551–1566. <https://doi.org/10.1029/2000WR900404>
- Hooper A, Zebker H, Segall P, Kampes B (2004) A new method for measuring deformation on volcanoes and other natural terrains using InSAR persistent scatterers. *Geophys Res Lett* 31:1–5. <https://doi.org/10.1029/2004GL021737>
- Hu B, Zhou J, Wang J, Chen Z, Wang D, Xu S (2009) Risk assessment of land subsidence at Tianjin coastal area in China. *Environ Earth Sci* 59(2):269–276. <https://doi.org/10.1007/s12665-009-0024-6>
- Hu R, Yue Z, Wang L, Wang S (2004) Review on current status and challenging issues of land subsidence in China. *Eng Geol* 76(1–2):65–77. <https://doi.org/10.1016/j.enggeo.2004.06.006>
- Jeanne P, Farr T, Rutqvist J, Vasco D (2019) Role of agricultural activity on land subsidence in the San Joaquin Valley, California. *J Hydrol* 569:462–469. <https://doi.org/10.1016/j.jhydrol.2018.11.077>
- Jia S, Wang H, Zhao S, Luo Y (2007) A tentative study of the mechanism of land subsidence in Beijing. *City Geol* 2(1):20–26. <https://doi.org/10.3969/j.issn.1007-1903.2007.01.005>
- Jia S, Ye C, Luo Y, Wang R, Tian F, Zhou Y, Yang Y, Liu M, Lei K, Li Y (2018) *Beijing Land Subsidence*. Geological Publishing House, Beijing
- Lei K, Luo Y, Chen B, Guo G, Zhou Y (2016) Distribution characteristics and influence factors of land subsidence in Beijing area. *Geology in China* 43(6):2216–2225. <https://doi.org/10.12029/gc20160628>
- Lei K, Luo Y, Liu H, Tian M, Wang X, Kong X, Sha T, Zhao L (2020) Land subsidence monitoring report of Beijing in 2019. Beijing: Beijing institute of Hydrogeology and Engineering Geology (Beijing Institute of Geo-Environment Monitoring)
- Lei K, Ma F, Luo Y, Chen B, Cui W, Tian F, Sha T (2022) The main subsidence layers and deformation characteristics in Beijing plain at present. *J EngGeol* 30(2):442–458. <https://doi.org/10.13544/j.cnki.jeg.2021-0238>
- Li X, Ye S, Wei A, Zhou P, Wang L (2017) Modelling the response of shallow groundwater levels to combined climate and water-diversion scenarios in Beijing-Tianjin-Hebei Plain. *China Hydrogeology Journal* 25(6):1733–1744. <https://doi.org/10.1007/s10040-017-1574-4>
- Liu Y, Helm D (2008a) Inverse procedure for calibrating parameters that control land subsidence caused by subsurface fluid withdrawal: 1. Methods *Water Resour Res* 44(7):W07423. <https://doi.org/10.1029/2007WR006605>
- Liu Y, Helm D (2008b) Inverse procedure for calibrating parameters that control land subsidence caused by subsurface fluid withdrawal: 2. Field Application *Water Resour Res* 44(7):W07424. <https://doi.org/10.1029/2007WR006606>
- Malinowska A, Witkowski W, Hejmanowski R, Chang L, Van L, Hanssen R (2019) Sinkhole occurrence monitoring over shallow abandoned coal mines with satellite-based persistent scatterer interferometry. *Eng Geol* 262:105336. <https://doi.org/10.1016/j.enggeo.2019.105336>
- Miller M, Shirzaei M (2015) Spatiotemporal characterization of land subsidence and uplift in Phoenix using InSAR time series and wavelet transforms. *J Geophys Res Solid Earth* 120(8):5822–5842
- Motagh M, Walter T, Sharifi M, Fielding E, Schenk A, Anderssohn J, Zschau J (2008) Land subsidence in Iran caused by widespread water reservoir overexploitation. *Geophys Res Lett* 35(16):1029–1039. <https://doi.org/10.1029/2008GL033814>
- Motagh M, Shamshiri R, Haghshenas Haghighi M, Wetzel H-U, Akbari B, Nahavandchi H, Roessner S, Arabi S (2017) Quantifying groundwater exploitation induced subsidence in the Rafsanshan plain, southeastern Iran, using InSAR time-series and in situ measurements. *Eng Geol* 218:134–151. <https://doi.org/10.1016/j.enggeo.2017.01.011>
- Ng H, Ge L, Li X, Zhang K (2012) Monitoring ground deformation in Beijing, China with persistent scatterer SAR interferometry. *J Geod* 86:375–392. <https://doi.org/10.1007/s00190-011-0525-4>
- Pacheco-Martínez J, Hernández-Martín M, Burbey T, González-Cervantes N, Ortiz-Lozano J, Zermeno De-Leona M, Solís-Pinto A (2013) Land subsidence and ground failure associated to groundwater exploitation in the Aguascalientes Valley, Mexico *Eng Geol* 164:172–186
- Pavelko M, Hoffmann J, Damar N (2006) Interferograms Showing Land Subsidence and Uplift in Las Vegas Valley, Nevada, 1992–99. U. S. Geological Survey, Reston, Virginia. <https://doi.org/10.3133/SIR20065218>
- Phien-Wej N, Giao P, Nutalaya P (2006) Land subsidence in Bangkok, Thailand. *Eng Geol* 82(4):187–201. <https://doi.org/10.1016/j.enggeo.2005.10.004>
- Riley F (1969) Analysis of borehole extensometer data from central California, Land Subsidence (Vol. 2). *Int Ass Sci Hydrol Publ* 89:423–432
- Shao X (2007) Fresh water thinking for a thirsty nation. *China Legal System (in Chinese)* 2:56–57
- Shi X, Xue Y, Wu J, Ye S, Zhang Y, Wei Z, Yu J (2008) Characterization of regional land subsidence in Yangtze Delta, China: the example of Su-Xi-Chang area and the city of Shanghai. *Hydrogeol J* 16(3):593–607. <https://doi.org/10.1007/s10040-007-0237-2>
- Strozzi T, Carreon-Freyre D, Wegmüller U (2020) Land subsidence and associated ground fracturing: study cases in central Mexico with ALOS-2 PALSAR-2 ScanSAR Interferometry. *Proc IAHS* 382:179–182. <https://doi.org/10.5194/piahs-382-179-2020>
- Strozzi T, Wegmüller U (1999) Land subsidence in Mexico City mapped by ERS differential SAR interferometry. *Geoscience and Remote Sensing Symposium, IGARSS '99 Proceedings*.

- IEEE 1999 International 4:1940–1942. <https://doi.org/10.1109/IGARSS.1999.774993>
- Teatini P, Strozzi T, Tosi L, Wegmüller U, Werner C, Carbognin L (2007) Assessing short- and long-time displacements in the Venice coastland by synthetic aperture radar interferometric point target analysis. *J Geophys Res* 112:F01012. <https://doi.org/10.1029/2006JF000656>
- Teatini P, Tosi L, Strozzi T, Carbognin L, Cecconi G, Rosselli R, Libardo S (2010) Resolving land subsidence within the Venice Lagoon by persistent scatterer SAR interferometry. *Physics and Chemistry of the Earth Parts a/b/c* 40:72–79. <https://doi.org/10.1016/j.pce.2010.01.002>
- Tomas R, Herrera G, Cooksley G, Mulas J (2011) Persistent scatterer interferometry subsidence data exploitation using spatial tools: the Vega media of the Segura river basin case study. *J Hydrol* 400(3–4):411–428. <https://doi.org/10.1016/j.jhydrol.2011.01.057>
- Tosi L, Teatini P, Carbognin L, Frankenfield J (2007) A new project to monitor land subsidence in the northern Venice coastland (Italy). *Environ Geol* 52(5):889–898. <https://doi.org/10.1007/s00254-006-0530-8>
- Wei T, Zhao X, Motagh M, Bi G, Li J, Chen M, Chen H, Liao M (2022) Land subsidence and rebound in the Taiyuan basin, northern China, in the context of inter-basin water transfer and groundwater management. *Remote Sens Environ* 269:112792. <https://doi.org/10.1016/j.rse.2021.112792>
- Wei W, Lv X, Cai X (2008) *Beijing Urban Geology*. China Land Press, Beijing
- Xu Y, Ma L, Du Y, Shen S (2012) Analysis of urbanisation-induced land subsidence in Shanghai. *Nat Hazards* 63(2):1255–1267. <https://doi.org/10.1007/s11069-012-0220-7>
- Xue Y, Yun Z, Ye S, Wu J, Li Q (2005) Land subsidence in China. *Environ Geol* 48(6):713–720. <https://doi.org/10.1007/s00254-005-0010-6>
- Yang Y, Li G, Dong Y, Li M, Yang J, Zhou D, Yang Z, Zheng F (2012) Influence of South to North Water Transfer on groundwater dynamic change in Beijing plain. *Environ Earth Sci* 65(4):1323–1331. <https://doi.org/10.1007/s12665-011-1381-5>
- Ye A, Duan Q, Chu W, Xu J, Mao Y (2014) The impact of the South-North Water Transfer Project (CTP)'s central route on groundwater table in the Hai River basin. *North China Hydrological Processes* 28(23):5755–5768. <https://doi.org/10.1002/hyp.10081>
- Ye S, Luo Y, Wu JC, Yan X, Wang H, Jiao X, Teatini P (2016a) Three-dimensional numerical modeling of land subsidence in Shanghai. *China Hydrogeol J* 24(3):695–709. <https://doi.org/10.1007/s10040-016-1382-2>
- Ye S, Xue Y, Wu J, Yan X, Yu J (2016b) Progression and mitigation of land subsidence in China[J]. *Hydrogeol J* 24:685–693. <https://doi.org/10.1007/s10040-015-1356-9>
- Zhang M, Hu L, Yao L, Yin W (2018) Numerical studies on the influences of the South-to-North Water transfer Project on groundwater level changes in the Beijing Plain. *China Hydrological Processes* 32(12):1858–1873. <https://doi.org/10.1002/hyp.13125>
- Zhang Y, Gong H, Gu Z, Wang R, Li X, Zhao W (2014) Characterization of land subsidence induced by groundwater withdrawals in the plain of Beijing city. *China Hydrogeol J* 22(2):397–409. <https://doi.org/10.1007/s10040-013-1069-x>
- Zhang Y, Wu H, Kang Y, Zhu C (2016) Ground subsidence in the Beijing-Tianjin-Hebei region from 1992 to 2014 revealed by multiple SAR stacks. *Remote Sens* 8:675. <https://doi.org/10.3390/rs8080675>
- Zhang Y, Wu J, Xue Y, Wang Z, Yao Y, Yan X, Wang H (2015) Land subsidence and uplift due to long-term groundwater extraction and artificial recharge in Shanghai. *China Hydrogeol J* 23(8):1851–1866. <https://doi.org/10.1007/s10040-015-1302-x>
- Zhang Y, Xue Y, Wu J, Wang H, He J (2012) Mechanical modeling of aquifer sands under long-term groundwater withdrawal. *Eng Geol* 125:74–80. <https://doi.org/10.1016/j.enggeo.2011.11.006>
- Zhang Y, Xue Y, Wu J, Ye S, Li Q (2007) Stress-strain measurements of deforming aquifer systems that underlie Shanghai. *China Eng Geol* 13(3):217–228. <https://doi.org/10.2113/gsegeosci.13.3.217>
- Zhao Y, Zhu Y, Lin Z, Wang J, He G, Li H, Li L, Wang H, Jiang S, He F, Zhai J, Wang L, Wang Q (2017) Energy reduction effect of the south-to-north water diversion project in China. *Sci Rep* 7(1):1–9. <https://doi.org/10.1038/s41598-017-16157-z>
- Zhu L, Gong H, Chen Y, Wang S, Ke Y, Guo G, Li X, Chen B, Wang H, Teatini P (2020) Effects of Water Diversion Project on groundwater system and land subsidence in Beijing. *China Eng Geol* 276:105763. <https://doi.org/10.1016/j.enggeo.2020.105763>
- Zhu L, Gong H, Li X, Wang R, Chen B, Dai Z, Teatini P (2015) Land subsidence due to groundwater withdrawal in the northern Beijing plain. *China Eng Geol* 193:243–255. <https://doi.org/10.1016/j.enggeo.2015.04.020>

Springer Nature or its licensor (e.g. a society or other partner) holds exclusive rights to this article under a publishing agreement with the author(s) or other rightsholder(s); author self-archiving of the accepted manuscript version of this article is solely governed by the terms of such publishing agreement and applicable law.